

Supplementary Information

Understanding and mitigating A-site surface enrichment in Ba-containing perovskites: a combined computational and experimental study of BaFeO₃

Jiapeng Liu^{a,1}, Jun Kyu Kim^{b,1}, Yuhao Wang^{a,1}, Hyunseung Kim^{b,1}, Alessio Belotti^a, Bonjae Koo^{b,†}, Zheng Wang^a, WooChul Jung^{b,*}, Francesco Ciucci^{a,c,d,e,*}

^a Department of Mechanical and Aerospace Engineering, The Hong Kong University of Science and Technology, Hong Kong, China

^b Department of Materials Science and Engineering, Korea Advanced Institute of Science and Technology (KAIST), Daejeon 34141, Republic of Korea

^c Department of Chemical and Biological Engineering, The Hong Kong University of Science and Technology, Hong Kong, China

^d HKUST Shenzhen-Hong Kong Collaborative Innovation Research Institute, Shenzhen, China

^e HKUST Energy Institute, The Hong Kong University of Science and Technology, Hong Kong, China

[†] Current address: School of Chemistry and Energy, Sungshin Women's University, Seoul 01133, Republic of Korea

* Corresponding E-mail: francesco.ciucci@ust.hk (Francesco Ciucci) wjung@kaist.ac.kr (WooChul Jung)

¹These authors contributed equally to this work.

1. Experimental methods

1.1. Powder synthesis

$\text{Ba}_{0.95}\text{La}_{0.05}\text{FeO}_{3-\delta}$ (BLF) and $\text{Ba}_{0.95}\text{La}_{0.05}\text{Fe}_{0.9}\text{Zr}_{0.1}\text{O}_{3-\delta}$ (BLFZ) were synthesized by a sol-gel complexing process. First, stoichiometric amounts of $\text{Ba}(\text{NO}_3)_2$ (Sigma Aldrich, >99%), $\text{La}(\text{NO}_3)_3$ (Sigma Aldrich, >99.9%), $\text{Fe}(\text{NO}_3)_3 \cdot 9\text{H}_2\text{O}$ (Sigma Aldrich, >98%), and $\text{ZrO}(\text{NO}_3)_2$ (35 wt. % in dilute nitric acid, Sigma Aldrich, $\geq 99\%$) were dissolved in deionized water. Ethylenediaminetetraacetic acid (EDTA) and citric acid (CA) were added as chelating agents in molar ratios of 1:1 and 2:1, respectively. After adjusting the pH to 6 with an aqueous solution of NH_3 , the mixture was stirred at 120 °C until a viscous gel was obtained. The gel was then calcined at 250 °C for 6 h, and the resulting powders were sintered for 12 h at 1200 °C. Then, the materials were iso-statically pressed at 300MPa and re-sintered for an additional 6 h at 1200 °C. The resulting dense round pellets were used as targets for the pulse laser deposition (PLD) process. Yttria-stabilized zirconia (YSZ) and NiO-YSZ powders were purchased from SOFCMAN, Ningbo, China. $\text{BaZr}_{0.1}\text{Ce}_{0.7}\text{Y}_{0.1}\text{Yb}_{0.1}\text{O}_{3-\delta}$ (BZCYYb) powders were synthesized according to the conventional solid-state reaction method reported in the literature¹. Stoichiometric amounts of BaCO_3 , ZrO_2 , CeO_2 , Y_2O_3 , and Yb_2O_3 (AR, Sinopharm Chemical Reagent Co., Ltd) were ball-milled for 48 h in ethanol. After drying, the powder was then sintered at 1100 °C for 10 h. After that, the ball-milling and sintering processes were repeated once more. NiO-BZCYYb powders were obtained by ball-milling NiO (55 wt%), BZCYYb (45 wt%), and corn starch (extra 15 wt%).

1.2. Basic Characterization

The powders were examined by X-ray diffraction (XRD, Empyrean PANalytical) with filtered Cu K-alpha radiation ($\lambda = 1.5406 \text{ \AA}$, 40 kV, 40 mA) for $10^\circ \leq 2\theta \leq 90^\circ$ at room temperature (RT). The resulting XRD patterns were Rietveld-refined using the X'Pert HighScore Plus

software. The composition of the bulk of the materials was verified by X-ray fluorescence (XRF) using the element analyzer JEOL JSX-3201Z.

1.3. Thin-film fabrication and characterization

The epitaxial thin-film samples of $\text{Ba}_{0.95}\text{La}_{0.05}\text{FeO}_{3-\delta}$ (BLF) and $\text{Ba}_{0.95}\text{La}_{0.05}\text{Fe}_{0.9}\text{Zr}_{0.1}\text{O}_{3-\delta}$ (BLFZ) were grown by pulsed laser deposition (PLD) from oxide targets of the respective materials and deposited onto (001)-oriented SrTiO_3 (STO) and (002)-oriented MgO single-crystal substrates (10 mm×10 mm×5 mm, MTI Corporation). An excimer laser (KrF with 248 nm wavelength, Coherent COMPex Pro 205) was used with an average energy of 270 mJ/pulse and with a repetition rate of 2 Hz. The substrates were heated to 700 °C during deposition, while the oxygen pressure was maintained at 10 mTorr after pumping the background pressure to 10^{-5} Torr. After thin-film deposition and prior to cooling, the samples were annealed in the same PLD chamber at 700 °C with 1 Torr of pure oxygen for 20 min. The resulting thin films had a thickness of approximately 25 nm. Polycrystalline BLF and BLFZ films were also fabricated on Si substrates in the same manner as epitaxial films but had a thickness of roughly 200 nm.

Both the in-plane and out-of-plane reflections of the deposited thin films on single-crystal STO (001) and MgO (002) substrates were measured by high-resolution thin-film X-ray diffraction (HR-XRD, X'Pert-PRO MRD, PANalytical) with Cu radiation (wavelength = 1.541 Å). The range of 2θ - ω scan for out-of-plane was 20° to 60° and that of in-plane (*e.g.* both (110)- and (100)- directions) was 20° to 90°. In-plane ϕ scans of all films were collected from the (200) plane in the range of 0° to 360°. The surface morphology of the thin-film samples was also characterized by atomic force microscopy (AFM, XE-100, Park Systems) in non-contact mode, and the data was analyzed through XEI software. Angle-resolved X-ray photoelectron spectroscopy (AR-XPS, Sigma Probe, Thermo Fisher Scientific) measurements were performed to obtain the surface chemical compositions of all thin films using monochromated

Al K α radiation (beam energy = 1486.6 eV) under ultrahigh vacuum with a standard detector. The range of emission angle was 0° to 60° (in the case of polycrystalline films, the range was 0° to 45°) with 15° intervals. All AR-XPS spectra were calibrated to the C-C bond (binding energy of 284.8 eV), and Shirley's background was used for quantitative analysis.

1.4. Electrical conductivity relaxation (ECR) measurements

Polycrystalline BLF and BLFZ thin films were deposited on c-Al₂O₃ substrates in the same manner as the epitaxial films. Thicknesses of 500 nm were achieved by increasing the PLD deposition time. Then, two, 1-mm-spaced Pt current collectors were deposited on the BLF and BLFZ films using a DC magnetron sputtering system, which was operated at 10 mTorr Ar and 100 W of DC power.

The ECR measurements were conducted at 550 – 650 °C in a tube furnace by switching the atmosphere between synthetic air ($p_{O_2} = 0.21$ atm) and pure oxygen ($p_{O_2} = 1$ atm). In detail, the samples were first stabilized at $p_{O_2} = 0.21$ atm and 650 °C, then the gas atmosphere was rapidly changed to $p_{O_2} = 1$ atm. After complete oxidation, the gas composition was switched back to synthetic air. Throughout the experiment, the in-plane current (or conductivity) was measured by chronoamperometry (CA, VSP-300, Biologic) at an applied DC voltage of 100 mV. Additional measurements were carried out at temperatures of 550 and 600 °C. To obtain the oxygen exchange coefficient, k_s , the electrical conductivity, $\sigma(t)$, at time t was regressed against the following first-order oxygen exchange model:

$$\frac{\sigma(t) - \sigma(0)}{\sigma(\infty) - \sigma(0)} = 1 - \exp\left(-\frac{k_s}{a} t\right)$$

where $a = 500$ nm is the thickness of either BLF or BLFZ films, $\sigma(0)$ and $\sigma(\infty)$ are the initial and relaxed electrical conductivities, respectively.

1.5. Electrochemical impedance spectroscopy (EIS) measurements

BLF and BLFZ ink slurries were prepared by ball-milling the respective perovskite powders with an ink vehicle (fuelcellmaterials) for 24 h. The electrode slurry was then screen-printed onto both sides of Sm-doped CeO₂ (1 cm × 1 cm and 350 μm thick) and annealed at 900 °C for 2 h.

The prepared BLF- and BLFZ-based symmetric cells were then placed inside a continuous-flow alumina tube into which synthetic air flowed at a rate of 100 sccm. In the $T = 450 - 650$ °C range, electrochemical impedance spectroscopy (EIS, VSP-300, Biologic) was performed. In the EIS measurement, the AC amplitude was set at 40 mV and the frequency range probed was from 10 mHz and 2 MHz with 81 points in logarithmic spacing. The impedance data was then used to estimate the polarization resistance. To document stability, the polarization resistance of the cell was measured for 50 h at 600 °C.

1.6. Fuel cell fabrication, performance, and morphology characterization

Anode-electrolyte pellets were obtained by co-pressing and co-sintering (1400 °C for 10 h) NiO-YSZ and YSZ (SOFC) and NiO-BZCYYb and BZCYYb (PCFC) powders. The cathode slurries (mixed BLFZ powder and V-737 binder from Heraeus) were first screen-printed on the electrolyte with an active area of 0.45 cm² and then sintered at 1150 °C for 5 h. The current-voltage (I-V) and current-power density (I-P) curves of the fuel cells were measured using a Keysight B2901A source meter in a two-probe configuration with a temperature range from 750 °C to 850 °C (SOFC) and 600 °C to 700 °C (PCFC). H₂ was fed into the anode and the cathode was exposed to ambient air. The morphology and structure of the button cells were studied using field-emission scanning electron microscopy (SEM, JSM-6390, JEOL).

1.7. First-principle calculations

All spin-polarized DFT calculations were performed using the Vienna *ab initio* simulation package (VASP)^{2, 3} with the projector-augmented wave (PAW) method⁴. The PAW

pseudopotentials with valence-electron configurations of $5s^25p^66s^2$ for Ba, $3p^63d^74s^1$ for Fe, $4s^24p^65s^24d^2$ for Zr, and $2s^22p^4$ for O were employed. The kinetic energy cutoff was set at 475 eV. To handle electron exchange correlations, the Perdew-Burk-Ernzerhof (PBE) functional⁵ under the generalized gradient approximation (GGA) scheme was used. The strongly correlated Fe-3d electrons were modeled using the DFT+U approach⁶ with the U_{eff} value set at 4.0 eV, consistent with previous studies on Fe-based perovskites⁷⁻⁹. The Brillouin zone was sampled using a Monkhorst-Pack scheme with a k -point grid of $6\times6\times6$ for the bulk computations and $6\times6\times1$ for the slab model. The structural relaxations were obtained using the conjugate gradient method with an energy convergence criterion within 10^{-5} eV and a force convergence factor on each atom of 0.02 eV/Å.

The primitive cell of BFO used for modeling the bulk and slab was taken to be cubic with a $\text{Pm}\bar{3}\text{m}$ space group consistent with experiments and previous calculations^{9, 10}. The bulk properties were simulated using a $2\times2\times2$ supercell, see Figure S1a. A nine-layer symmetric slab, see Figure S1b, was used as the surface model. Such a symmetric configuration was used to remove the presence of the fictitious dipole moment. A vacuum layer of 16 Å along the c direction was added to minimize self-interactions. Six identical slab models with different plane-indexes and terminations, *i.e.*, (001) BaO, (001) FeO₂, (110) BaFeO, (110) O₂, (111) BaO₃, and (111) Fe, were studied. For each slab model, the top three (I, II, and III) and bottom three (I symm, II symm, and III symm) layers, see Figure S1b, were allowed to relax while the middle three layers (IV, mirror, IV symm) were fixed to simulate the bulk of the material.

1.8. Surface phase diagram

In this section, we illustrate how the thermodynamic surface phase diagram of BFO was constructed. The diagram depends on the chemical potentials of Ba and O. Further, it allows us to determine the conditions for which Ba metal and Fe metal and related oxides do not

precipitate, *i.e.*, a certain BFO termination is stable. To be specific, the construction procedure starts by computing the chemical potentials for which the surface of BFO is at equilibrium with both the bulk of the material and the surrounding atmosphere. The sum of the chemical potentials of the Ba (μ_{Ba}), Fe (μ_{Fe}), and O (μ_{O}) in bulk equals the Gibbs free energy, $g_{\text{BFO}}^{\text{bulk}}$, of BFO. Following the literature, we assumed that the vibrational entropy contributions to the Gibbs free energy are negligible.¹¹ Therefore, the $g_{\text{BFO}}^{\text{bulk}}$ can be approximated by the ground-state energy, $E_{\text{BFO}}^{\text{bulk}}$, of the BFO crystal. In other words, the following holds:

$$\mu_{\text{Ba}} + \mu_{\text{Fe}} + 3\mu_{\text{O}} = g_{\text{BFO}}^{\text{bulk}} \approx E_{\text{BFO}}^{\text{bulk}} \quad (\text{S1})$$

This constraint allowed us to determine the surface phase diagram as a function of only two variables out of μ_{Ba} , μ_{Fe} , and μ_{O} . In the phase diagram, instead of using μ_{Ba} , μ_{Fe} , and μ_{O} , we used the following chemical potential differences for Ba, Fe, and O:

$$\Delta\mu_{\text{Ba}} = \mu_{\text{Ba}} - E_{\text{Ba}}^{\text{bulk}} \quad (\text{S2a})$$

$$\Delta\mu_{\text{Fe}} = \mu_{\text{Fe}} - E_{\text{Fe}}^{\text{bulk}} \quad (\text{S2b})$$

$$\Delta\mu_{\text{O}} = \mu_{\text{O}} - \frac{E_{\text{O}_2}}{2} \quad (\text{S2c})$$

where $E_{\text{Ba}}^{\text{bulk}}$ and $E_{\text{Fe}}^{\text{bulk}}$ are the ground state energies per atom of Ba metal and Fe metal, respectively, and E_{O_2} is the energy of an isolated O₂ molecule. For this work, we chose $\Delta\mu_{\text{Ba}}$ and $\Delta\mu_{\text{O}}$ to be the two independent variables.

To evaluate the surface stability, we used slab models and computed the surface Gibbs free energy, Ω , which is defined as the Gibbs free energy of a semi-infinite crystal in contact with an oxygen atmosphere reservoir¹¹⁻¹⁷. Hereafter, we use the superscript i to identify a specific slab with a specific termination, *i.e.*, i can designate (001) BaO, (001) FeO₂, *etc.* The Ω of the i -terminated slab is defined as the area-normalized difference between the total energy of the slab, E_{slab}^i , and the chemical potentials of its constituents^{12, 16, 17}

$$\Omega^i = \frac{1}{2A^i} (E_{\text{slab}}^i - N_{\text{Ba}}^i \mu_{\text{Ba}} - N_{\text{Fe}}^i \mu_{\text{Fe}} - N_{\text{O}}^i \mu_{\text{O}}) \quad (\text{S3})$$

where N_{Ba}^i , N_{Fe}^i , and N_{O}^i are the number of Ba, Fe, and O atoms in the i -terminated slab, respectively, and A^i is its surface area.

By substituting μ_{Ba} , μ_{Fe} , and μ_{O_2} from the (S2) in (S3), the Ω^i can be rewritten as

$$\Omega^i = \frac{1}{A^i} (\phi^i - \Gamma_{\text{Ba,Fe}}^i \Delta\mu_{\text{Ba}} - \Gamma_{\text{O,Fe}}^i \Delta\mu_{\text{O}}) \quad (\text{S4})$$

where

$$\Gamma_{a,\text{Fe}}^i = \frac{1}{2} \left(N_a^i - N_{\text{Fe}}^i \frac{N_a^{\text{bulk}}}{N_{\text{Fe}}^{\text{bulk}}} \right) \quad (\text{S5a})$$

$$\phi^i = \frac{1}{2} (E_{\text{slab}}^i - N_{\text{Fe}}^i E_{\text{BFO}}^{\text{bulk}}) - \Gamma_{\text{Ba,Fe}}^i E_{\text{Ba}}^{\text{bulk}} - \frac{1}{2} \Gamma_{\text{O,Fe}}^i E_{\text{O}_2} \quad (\text{S5b})$$

In the last two equations, $\Gamma_{a,\text{Fe}}^i$ denotes the excess of atoms a (Ba, Fe, or O) relative to Fe in the i -terminated slab, N_a^i and N_a^{bulk} represent the number of atoms a (Ba, Fe, or O) in the slab and the primitive cell, respectively, and ϕ^i is a scalar dependent on the specific termination i . For a detailed derivation of (S4) and (S5), refer to the following Section 1.9.

Following thermodynamics, $\Omega^i < 0$ implies that the i -terminated slab is unstable¹⁸. In contrast, an i -terminated slab is stable if $\Omega^i \geq 0$ ¹⁹. Consequently, a non-negative Ω^i is needed to ensure the integrity of the crystal structure. In order to obtain the range of allowed values for $\Delta\mu_{\text{Ba}}$ and $\Delta\mu_{\text{Fe}}$, we assumed that Ba and Fe do not precipitate on the BFO surface. Consequently, the chemical potential of Ba (μ_{Ba}) and Fe (μ_{Fe}) in the BFO need to be smaller than the energy of the corresponding metals, leading to the following constraints:

$$\Delta\mu_{\text{Ba}} < 0 \quad (\text{S6a})$$

$$\Delta\mu_{\text{Fe}} < 0 \quad (\text{S6b})$$

Further, to prevent the precipitation of M_xO_y ($M = \text{Ba}$, or Fe), the stoichiometrically weighted sum of μ_M and μ_O need to be smaller than the Gibbs free energy, $g_{M_xO_y}^{\text{bulk}}$, of M_xO_y . Such a constraint can be written as

$$x\Delta\mu_M + y\Delta\mu_O < E_{M_xO_y}^f \quad (\text{S7})$$

where $E_{M_xO_y}^f$ is the formation energy of the oxide M_xO_y defined as

$$E_{M_xO_y}^f = E_{M_xO_y}^{\text{bulk}} - xE_M^{\text{bulk}} - \frac{y}{2}E_{O_2} \quad (\text{S8})$$

For a detailed derivation of (S6) and (S7), refer to the following Section 1.10. We must point out that (S6) and (S7) can be rewritten using the variables $\Delta\mu_{\text{Ba}}$ and $\Delta\mu_O$, as shown in the following Section 1.10. In summary, the inequalities (S6) and (S7) define the conditions for which BFO is stable against the precipitation of Ba and Fe metal and corresponding oxides.

The equations presented up to this point refer to the ground state, where the temperature, T , and all pressures, p , are at their absolute zero. However, SOFC operates at finite T and p . This dependence can be included by rewriting the $\Delta\mu_O$ as $\Delta\mu_O(T, p_{O_2})$ ^{19, 20}, using

$$\begin{aligned} \Delta\mu_O(T, p_{O_2}) = & \frac{1}{2} \left[H_{O_2}^{\text{gas}}(T, p^0) - H_{O_2}^{\text{gas}}(T^0, p^0) - TS_{O_2}^{\text{gas}}(T, p^0) + T^0 S_{O_2}^{\text{gas}}(T^0, p^0) \right. \\ & \left. + k_B T \ln \left(\frac{p_{O_2}}{p_0} \right) \right] + \delta\bar{\mu}_O^0 \end{aligned} \quad (\text{S9})$$

where $T^0 = 298.15$ K, $p^0 = 1$ atm, k_B is the Boltzmann constant, p_{O_2} is the partial pressure of oxygen, and $H_{O_2}^{\text{gas}}$ and $S_{O_2}^{\text{gas}}$ are O_2 's experimental enthalpy and entropy, which can be determined from thermodynamic tables²¹. The last term, $\delta\bar{\mu}_O^0$ accounts for the difference between the experimental and the computational oxide formation energies. For a detailed derivation of (S9) and the calculation of $\delta\bar{\mu}_O^0$, refer to the following Section 1.11. As we can observe, $\Delta\mu_O$ correlates with p_{O_2} and T . Therefore, p_{O_2} and T can affect the Ω^i , thereby affecting the stability of different surfaces.

In summary, the thermodynamic surface phase diagram was constructed as a function of $\Delta\mu_{\text{Ba}}$ and $\Delta\mu_{\text{O}}$. The region for which a BFO slab of materials is stable is found by intersecting the regions in the $\Delta\mu_{\text{Ba}}, \Delta\mu_{\text{O}}$ space for which: 1) Ba and Fe metals do not precipitate as metals (*i.e.* inequalities (S6)); 2) all oxides of Ba and Fe do not precipitate (*i.e.* inequalities (S7)); 3) a BFO termination is stable (we can find at least one i for which $\Omega^i \geq 0$).

1.9. Derivation of the surface Gibbs free energy

In this section, we show how the surface Gibbs free energy, Ω^i , of the i -terminated slab, is derived.

After rewriting the equation (S1) as

$$\mu_{\text{Fe}} = E_{\text{BFO}}^{\text{bulk}} - \mu_{\text{Ba}} - 3\mu_{\text{O}} \quad (\text{S10})$$

we can substitute the μ_{Fe} in the definition of Ω^i , see (S3), and obtain Ω^i as a function of the chemical potentials μ_{Ba} and μ_{O} :

$$\Omega^i = \frac{1}{2A^i} [E_{\text{slab}}^i - N_{\text{Ba}}^i \mu_{\text{Ba}} - N_{\text{Fe}}^i (E_{\text{BFO}}^{\text{bulk}} - \mu_{\text{Ba}} - 3\mu_{\text{O}}) - N_{\text{O}}^i \mu_{\text{O}}] \quad (\text{S11})$$

The latter can be rearranged as

$$\Omega^i = \frac{1}{A^i} \left[\frac{E_{\text{slab}}^i - N_{\text{Fe}}^i E_{\text{BFO}}^{\text{bulk}}}{2} - \frac{1}{2} (N_{\text{Ba}}^i - N_{\text{Fe}}^i) \mu_{\text{Ba}} - \frac{1}{2} (N_{\text{O}}^i - 3N_{\text{Fe}}^i) \mu_{\text{O}} \right] \quad (\text{S12})$$

Let us define $\Gamma_{a,\text{Fe}}^i$, the excess of a relative to Fe in the slab, as

$$\Gamma_{a,\text{Fe}}^i = \frac{1}{2} \left(N_a^i - N_{\text{Fe}}^i \frac{N_a^{\text{bulk}}}{N_{\text{Fe}}^{\text{bulk}}} \right) \quad (\text{S13})$$

where a is either Ba or O, and N_a^i and N_a^{bulk} are the number of a atoms in the slab and bulk crystal, respectively. (S13) will allow us to define

$$\Gamma_{\text{Ba,Fe}}^i = \frac{1}{2}(N_{\text{Ba}}^i - N_{\text{Fe}}^i) \quad (\text{S14a})$$

$$\Gamma_{\text{O,Fe}}^i = \frac{1}{2}(N_{\text{O}}^i - 3N_{\text{Fe}}^i) \quad (\text{S14b})$$

Next, we introduce the chemical potential difference defined in equation (S2) and (S14) into (S12), and the Ω^i can be written as

$$\begin{aligned} \Omega^i &= \frac{1}{A^i} \left[\frac{E_{\text{slab}}^i - N_{\text{Fe}}^i E_{\text{BFO}}^{\text{bulk}}}{2} - \Gamma_{\text{Ba,Fe}}^i (\Delta\mu_{\text{Ba}} + E_{\text{Ba}}^{\text{bulk}}) - \Gamma_{\text{O,Fe}}^i \left(\Delta\mu_{\text{O}} + \frac{E_{\text{O}_2}}{2} \right) \right] \\ &= \frac{1}{A^i} \left[\left(\frac{E_{\text{slab}}^i - N_{\text{Fe}}^i E_{\text{BFO}}^{\text{bulk}}}{2} - \Gamma_{\text{Ba,Fe}}^i E_{\text{Ba}}^{\text{bulk}} - \Gamma_{\text{O,Fe}}^i \frac{E_{\text{O}_2}}{2} \right) - \Gamma_{\text{Ba,Fe}}^i \Delta\mu_{\text{Ba}} - \Gamma_{\text{O,Fe}}^i \Delta\mu_{\text{O}} \right] \end{aligned} \quad (\text{S15})$$

If we define

$$\phi^i = \frac{E_{\text{slab}}^i - N_{\text{Fe}}^i E_{\text{BFO}}^{\text{bulk}}}{2} - \Gamma_{\text{Ba,Fe}}^i E_{\text{Ba}}^{\text{bulk}} - \Gamma_{\text{O,Fe}}^i \frac{E_{\text{O}_2}}{2} \quad (\text{S16})$$

we can shorten (S15) and obtain (S4)

$$\Omega^i = \frac{1}{A^i} (\phi^i - \Gamma_{\text{Ba,Fe}}^i \Delta\mu_{\text{Ba}} - \Gamma_{\text{O,Fe}}^i \Delta\mu_{\text{O}}) \quad (\text{S17})$$

1.10. Inequalities constraining the precipitation of metals and metal oxides

In this section, we show how to obtain the constraints used to identify the precipitations of specific compounds, see equation (S8). We first define the formation energy, $E_{\text{M}_x\text{O}_y}^{\text{f}}$, of the oxide M_xO_y (where $\text{M} = \text{Ba}, \text{Fe}$) as

$$E_{\text{M}_x\text{O}_y}^{\text{f}} = E_{\text{M}_x\text{O}_y}^{\text{bulk}} - xE_{\text{M}}^{\text{bulk}} - \frac{y}{2}E_{\text{O}_2} \quad (\text{S18})$$

where $E_{\text{M}_x\text{O}_y}^{\text{bulk}}$ and $E_{\text{M}}^{\text{bulk}}$ are the ground state energies of the oxide and the metal M per formula unit. Similarly, the formation energy of BFO ($E_{\text{BFO}}^{\text{f}}$) can be calculated as

$$E_{\text{BFO}}^f = E_{\text{BFO}}^{\text{bulk}} - E_{\text{Ba}}^{\text{bulk}} - E_{\text{Fe}}^{\text{bulk}} - \frac{3}{2}E_{\text{O}_2} \quad (\text{S19})$$

Substituting equation (S1) into (S19), the E_{BFO}^f can be rewritten as

$$\begin{aligned} E_{\text{BFO}}^f &= \mu_{\text{Ba}} + \mu_{\text{Fe}} + 3\mu_{\text{O}} - E_{\text{Ba}}^{\text{bulk}} - E_{\text{Fe}}^{\text{bulk}} - \frac{3}{2}E_{\text{O}_2} \\ &= \Delta\mu_{\text{Ba}} + \Delta\mu_{\text{Fe}} + 3\Delta\mu_{\text{O}} \end{aligned} \quad (\text{S20})$$

The latter equation allows us to write the $\Delta\mu_{\text{Fe}}$ as a function of the two independent variables $\Delta\mu_{\text{Ba}}$ and $\Delta\mu_{\text{O}}$ as

$$\Delta\mu_{\text{Fe}} = E_{\text{BFO}}^f - \Delta\mu_{\text{Ba}} - 3\Delta\mu_{\text{O}} \quad (\text{S21})$$

The precipitation of Ba and Fe metals onto the surface of BFO is prevented if the chemical potentials of Ba and Fe in the BFO bulk crystal are less than the Gibbs free energy of corresponding metals, *i.e.*,

$$\mu_{\text{Ba}} < g_{\text{Ba}}^{\text{bulk}} \quad (\text{S22a})$$

$$\mu_{\text{Fe}} < g_{\text{Fe}}^{\text{bulk}} \quad (\text{S22b})$$

where $g_{\text{Ba}}^{\text{bulk}}$ and $g_{\text{Fe}}^{\text{bulk}}$ are the Gibbs free energy of Ba and Fe in their respective metal phase.

Similarly, the precipitation of M_xO_y does not occur if

$$x\mu_{\text{M}} + y\mu_{\text{O}} < g_{\text{M}_x\text{O}_y}^{\text{bulk}} \quad (\text{S23})$$

where μ_{M} is the chemical potential of metal M (M = Ba, Fe), $g_{\text{M}_x\text{O}_y}^{\text{bulk}}$ is the Gibbs free energy of the oxide M_xO_y . We should note that, as stated in the text, the contribution of the vibrational entropy to the Gibbs free energy is assumed to be negligible¹¹. This allowed us to approximate the $g_{\text{M}_x\text{O}_y}^{\text{bulk}}$, $g_{\text{Ba}}^{\text{bulk}}$, and $g_{\text{Fe}}^{\text{bulk}}$ using the $E_{\text{M}_x\text{O}_y}^{\text{bulk}}$, $E_{\text{Ba}}^{\text{bulk}}$, and $E_{\text{Fe}}^{\text{bulk}}$, respectively.

Substituting in (S23) the chemical potential difference defined in equation (S2) allows us to rewrite the inequalities (S22) and (S23) as

$$\Delta\mu_{\text{Ba}} = \mu_{\text{Ba}} - E_{\text{Ba}}^{\text{bulk}} < 0 \quad (\text{S24a})$$

$$\Delta\mu_{\text{Fe}} = \mu_{\text{Fe}} - E_{\text{Fe}}^{\text{bulk}} < 0 \quad (\text{S24b})$$

$$x\Delta\mu_{\text{M}} + y\Delta\mu_{\text{O}} < E_{\text{M}_x\text{O}_y}^{\text{bulk}} - xE_{\text{M}}^{\text{bulk}} - \frac{y}{2}E_{\text{O}_2} = E_{\text{M}_x\text{O}_y}^{\text{f}} \quad (\text{S24c})$$

which are equations (S7) and (S8).

Substituting in (S24b) the (S21) allows us to rewrite the Fe non-precipitation constraint as

$$E_{\text{BFO}}^{\text{f}} - \Delta\mu_{\text{Ba}} - 3\Delta\mu_{\text{O}} < 0 \quad (\text{S25})$$

The inequalities (S24c) can be written explicitly for BaO, BaO₂, Fe₂O₃, and FeO following

$$\Delta\mu_{\text{Ba}} + \Delta\mu_{\text{O}} < E_{\text{BaO}}^{\text{f}} \quad (\text{S26a})$$

$$\Delta\mu_{\text{Ba}} + 2\Delta\mu_{\text{O}} < E_{\text{BaO}_2}^{\text{f}} \quad (\text{S26b})$$

$$2\Delta\mu_{\text{Fe}} + 3\Delta\mu_{\text{O}} < E_{\text{Fe}_2\text{O}_3}^{\text{f}} \quad (\text{S26c})$$

$$\Delta\mu_{\text{Fe}} + \Delta\mu_{\text{O}} < E_{\text{FeO}}^{\text{f}} \quad (\text{S26d})$$

By replacing the $\Delta\mu_{\text{Fe}}$ in the (S26c) and (S26d) with (S21), the last two equations can be written as

$$2\Delta\mu_{\text{Ba}} + 3\Delta\mu_{\text{O}} > 2E_{\text{BFO}}^{\text{f}} - E_{\text{Fe}_2\text{O}_3}^{\text{f}} \quad (\text{S27a})$$

$$\Delta\mu_{\text{Ba}} + 2\Delta\mu_{\text{O}} > E_{\text{BFO}}^{\text{f}} - E_{\text{FeO}}^{\text{f}} \quad (\text{S27b})$$

To conclude, the precipitation of Ba and Fe metals is prevented if (S24a) and (S25) are satisfied. Similarly, BaO, BaO₂, Fe₂O₃, and FeO do not precipitate if (S26a), (S26b), (S27a), and (S27b) are satisfied.

1.11. Correction of temperature and oxygen partial pressure

To better correlate the first-principles simulation results with experiments, we included the corrections by finite temperature, T , and oxygen partial pressure, p_{O_2} , on the surface phase diagram. It is assumed that the surfaces are in equilibrium with the surrounding atmosphere, thus the chemical potential of oxygen, μ_{O} , should be identical to the one in its gas phase at specific T and p_{O_2} . The dependence can be written as

$$\mu_{\text{O}}(T, p_{\text{O}_2}) = \frac{1}{2} \left[E_{\text{O}_2} + \mu_{\text{O}_2}(T, p^0) + k_{\text{B}} T \ln \left(\frac{p_{\text{O}_2}}{p_0} \right) \right] \quad (\text{S28})$$

where $p^0 = 1$ atm, k_{B} is the Boltzmann constant, and $\mu_{\text{O}_2}(T, p^0)$ has the following expression

$$\mu_{\text{O}_2}(T, p^0) = H_{\text{O}_2}^{\text{gas}}(T, p^0) - H_{\text{O}_2}^{\text{gas}}(T^0, p^0) - T S_{\text{O}_2}^{\text{gas}}(T, p^0) + T^0 S_{\text{O}_2}^{\text{gas}}(T^0, p^0) \quad (\text{S29})$$

where $T^0 = 298.15$ K, and $H_{\text{O}_2}^{\text{gas}}$ and $S_{\text{O}_2}^{\text{gas}}$ correspond to the experimental enthalpy and entropy of O_2 gas. Therefore, $\Delta\mu_{\text{O}}(T, p_{\text{O}_2})$ can be rewritten as

$$\begin{aligned} \Delta\mu_{\text{O}}(T, p_{\text{O}_2}) &= \mu_{\text{O}}(T, p_{\text{O}_2}) - \frac{E_{\text{O}_2}}{2} = \frac{1}{2} \left[\mu_{\text{O}_2}(T, p^0) + k_{\text{B}} T \ln \left(\frac{p_{\text{O}_2}}{p_0} \right) \right] \\ &= \frac{1}{2} \left[H_{\text{O}_2}^{\text{gas}}(T, p^0) - H_{\text{O}_2}^{\text{gas}}(T^0, p^0) - T S_{\text{O}_2}^{\text{gas}}(T, p^0) \right. \\ &\quad \left. + T^0 S_{\text{O}_2}^{\text{gas}}(T^0, p^0) + k_{\text{B}} T \ln \left(\frac{p_{\text{O}_2}}{p_0} \right) \right] \end{aligned} \quad (\text{S30})$$

To account for the difference between the experimental formation enthalpy ($\Delta H_{f, \text{M}_x\text{O}_y}^0$) and the computational one for the metal oxide M_xO_y , one correction term $\delta\bar{\mu}_0^0$ will be added for $\Delta\mu_{\text{O}}(T, p)$. The $\delta\bar{\mu}_0^0$ is calculated as follows^{18, 20}

$$\begin{aligned} \delta\bar{\mu}_0^0 &= \frac{1}{m} \sum_{k=1}^m \left[\frac{1}{y_k} \left(E_{\text{M}_{x_k}\text{O}_{y_k}}^{\text{bulk}} - x_k E_{\text{M}}^{\text{bulk}} - \Delta H_{f, \text{M}_{x_k}\text{O}_{y_k}}^0 \right) \right. \\ &\quad \left. - \frac{1}{2} \left(E_{\text{O}_2} + T^0 S_{\text{O}_2}^{\text{gas}}(T^0, p^0) \right) \right] \end{aligned} \quad (\text{S31})$$

where $m = 4$ denotes the total number of oxides considered here, *i.e.* BaO, BaO₂, Fe₂O₃, and FeO, and x_k, y_k are used to clarify the different stoichiometries in different oxides.

Finally, the dependence of temperature and pressure are accounted in the $\Delta\mu_0$ as

$$\begin{aligned} \Delta\mu_0(T, p_{O_2}) = & \frac{1}{2} \left[H_{O_2}^{\text{gas}}(T, p^0) - H_{O_2}^{\text{gas}}(T^0, p^0) - TS_{O_2}^{\text{gas}}(T, p^0) + T^0 S_{O_2}^{\text{gas}}(T^0, p^0) \right. \\ & \left. + k_B T \ln \left(\frac{p_{O_2}}{p_0} \right) \right] + \delta\bar{\mu}_0^0 \end{aligned} \quad (\text{S32})$$

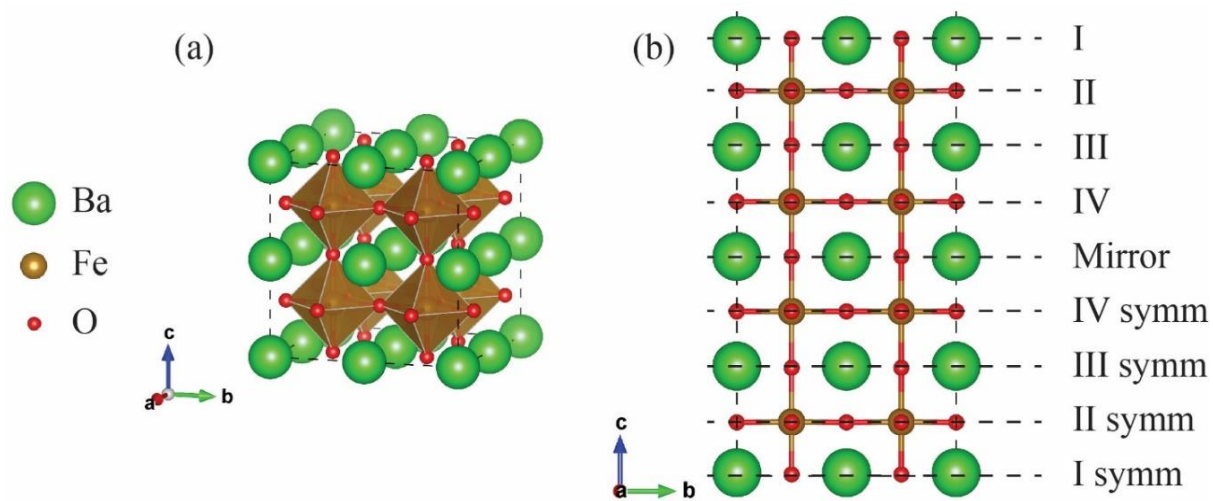


Figure S1 Schematic of the (a) $2 \times 2 \times 2$ supercell and (b) nine-layer symmetric slab model used for the bulk and surface calculations, respectively. The mirror plane is also labeled.

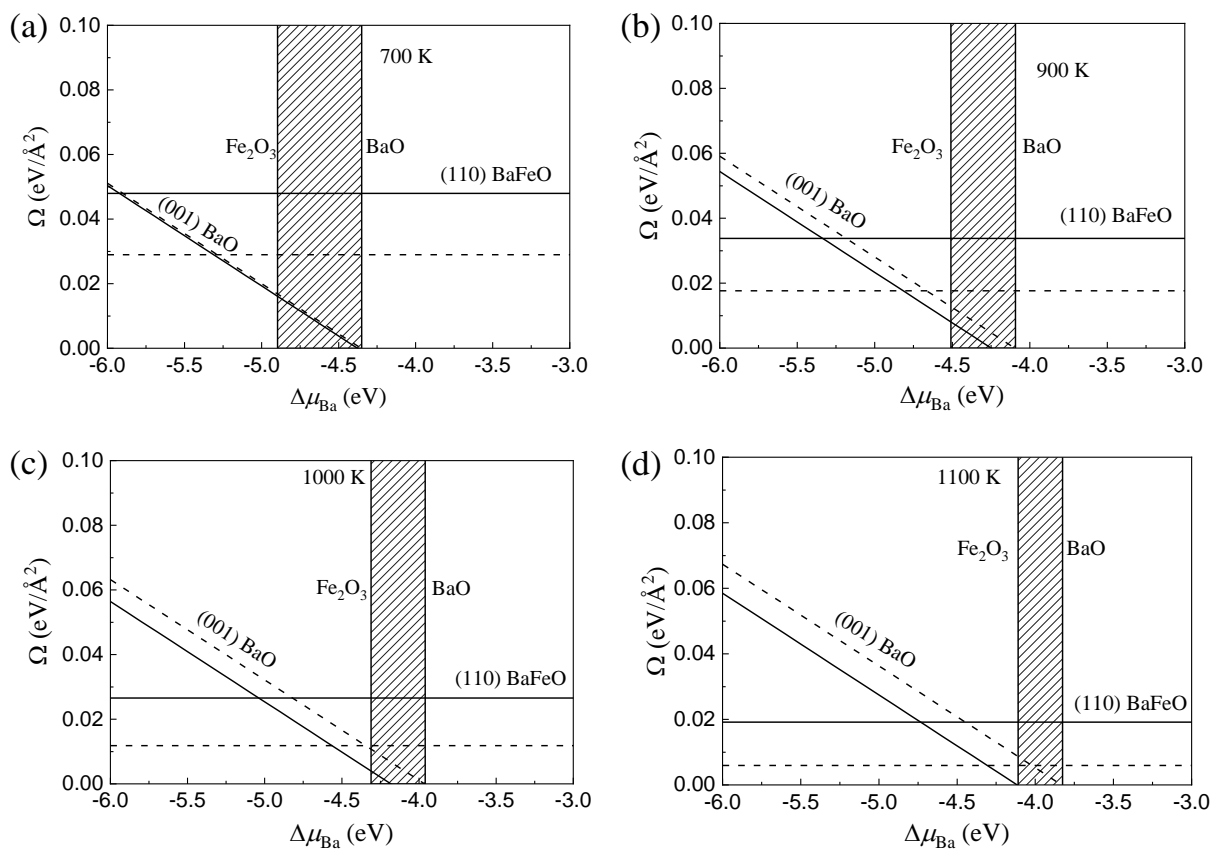


Figure S2 Surface Gibbs free energy Ω^i at ambient pressure and (a) 700 K, (b) 900 K, (c) 1000 K, and (d) 1100 K with O vacant sites at the sublayer. The dashed lines correspond to Ω^i with no O vacancies.

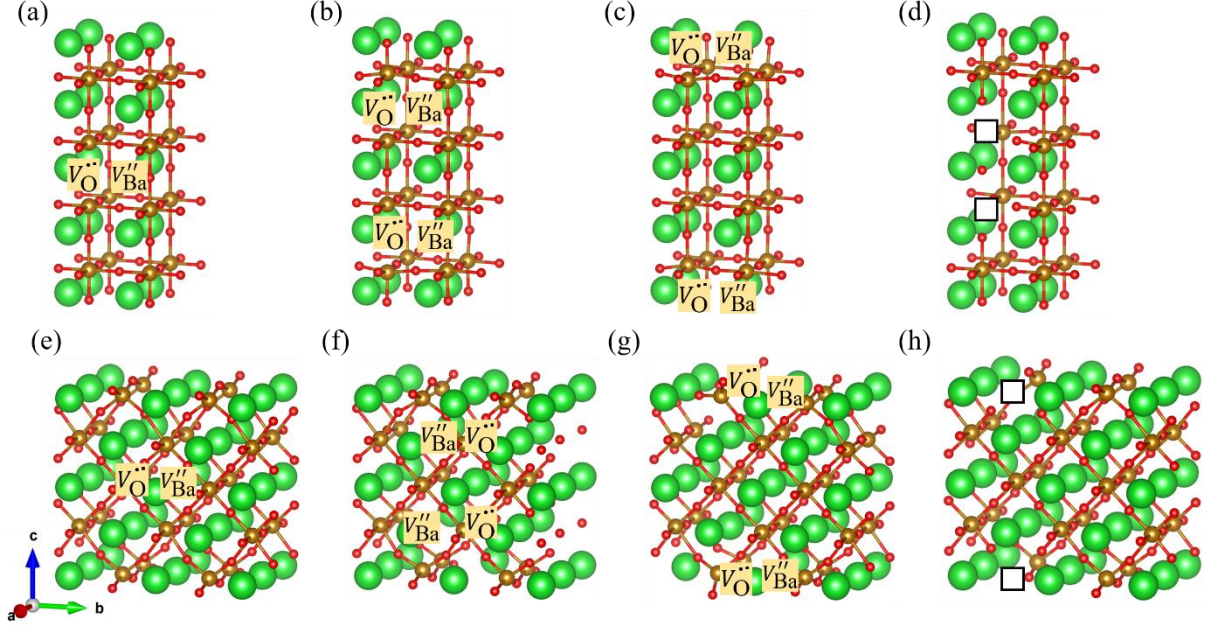


Figure S3 Optimized slab models of (a-d) (001) BaO and (e-h) (110) BaFeO with (a-c, e-g) one pair of Schottky defect of $V_{\text{Ba}}'' - V_{\text{O}}''$ and (d, h) Fe vacancy. Different locations for the defect pair of $V_{\text{Ba}}'' - V_{\text{O}}''$ were considered, (a) and (e) in the bulk (mirror plane), (b) and (f) in the layer III, (c) and (g) in the top surface (layer I). Here, two pairs of $V_{\text{Ba}}'' - V_{\text{O}}''$ in (b-c, f-g) and two Fe vacant sites in (d, h) were created to ensure the symmetry of the slab model.

The Schottky formation energy is calculated as

$$E_{\text{Schottky}} = E_{\text{slab}}^{\text{defect}} - E_{\text{slab}}^i + nE_{\text{BaO}}^{\text{bulk}} \quad (\text{S33})$$

where $E_{\text{slab}}^{\text{defect}}$ is the energy of slab with one pair of Schottky defect of $V_{\text{Ba}}'' - V_{\text{O}}''$, E_{slab}^i is the energy of the perfect slab, *i.e.*, (001) BaO and (110) BaFeO, as calculated before, $E_{\text{BaO}}^{\text{bulk}}$ is the energy of BaO per formula unit in its face-centered cubic phase, and n is the pair of defects removed.

The vacancy formation energy of Fe, $E_{\text{Fe,vac}}$, can be computed using the following formula:

$$E_{\text{Fe,vac}} = \frac{(E_{\text{slab}}^{\text{defect}} + 2E_{\text{Fe}}^{\text{bulk}}) - E_{\text{slab}}^{\text{perfect}}}{2} \quad (\text{S34})$$

where $E_{\text{slab}}^{\text{defect}}$ and $E_{\text{slab}}^{\text{perfect}}$ are the energies of the slab with and without Fe vacancies, respectively, and $E_{\text{Fe}}^{\text{bulk}}$ is the energy of Fe per atom in its body-centered cubic phase. As shown in Figure S3d and Figure S3h, the sites that favor Fe vacancy formation are found in the bulk of the (001) BaO-terminated slab (layer IV and IV symm) and in the topmost surface of (110) BaFeO-terminated slab (layer I and I symm). The $E_{\text{Fe,vac}}$ values were predicted to be 7.40 and 3.28 eV for (001) BaO- and (110) BaFeO-terminated slabs, respectively, implying that the formation of Fe vacancies is significantly less likely than oxygen vacancies.

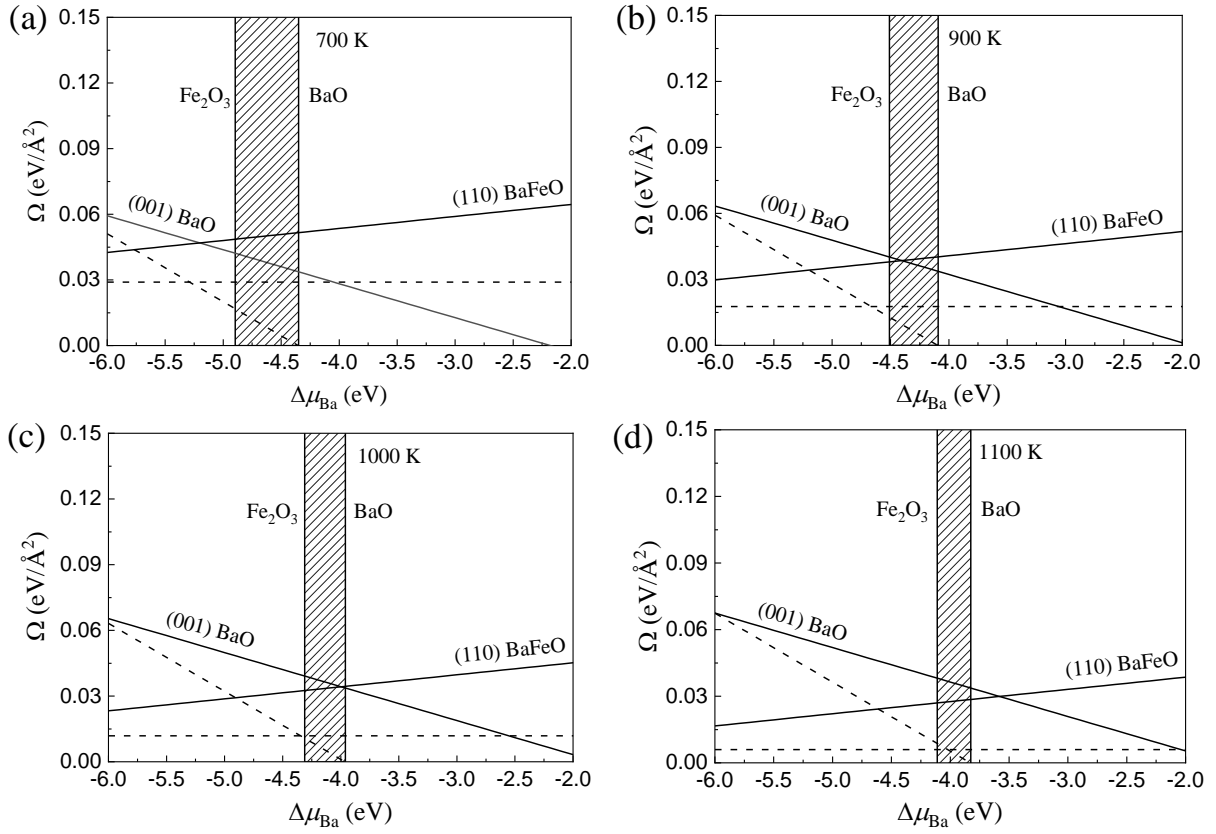


Figure S4 Surface Gibbs free energy Ω^i at ambient pressure and (a) 700 K, (b) 900 K, (c) 1000 K, and (d) 1100 K with Schottky defects of $V_{\text{Ba}}'' - V_{\text{O}}''$ in the (001) BaO and (110) BaFeO terminated slabs. The dashed lines correspond to the surface Gibbs free energy without the Schottky defect pair.

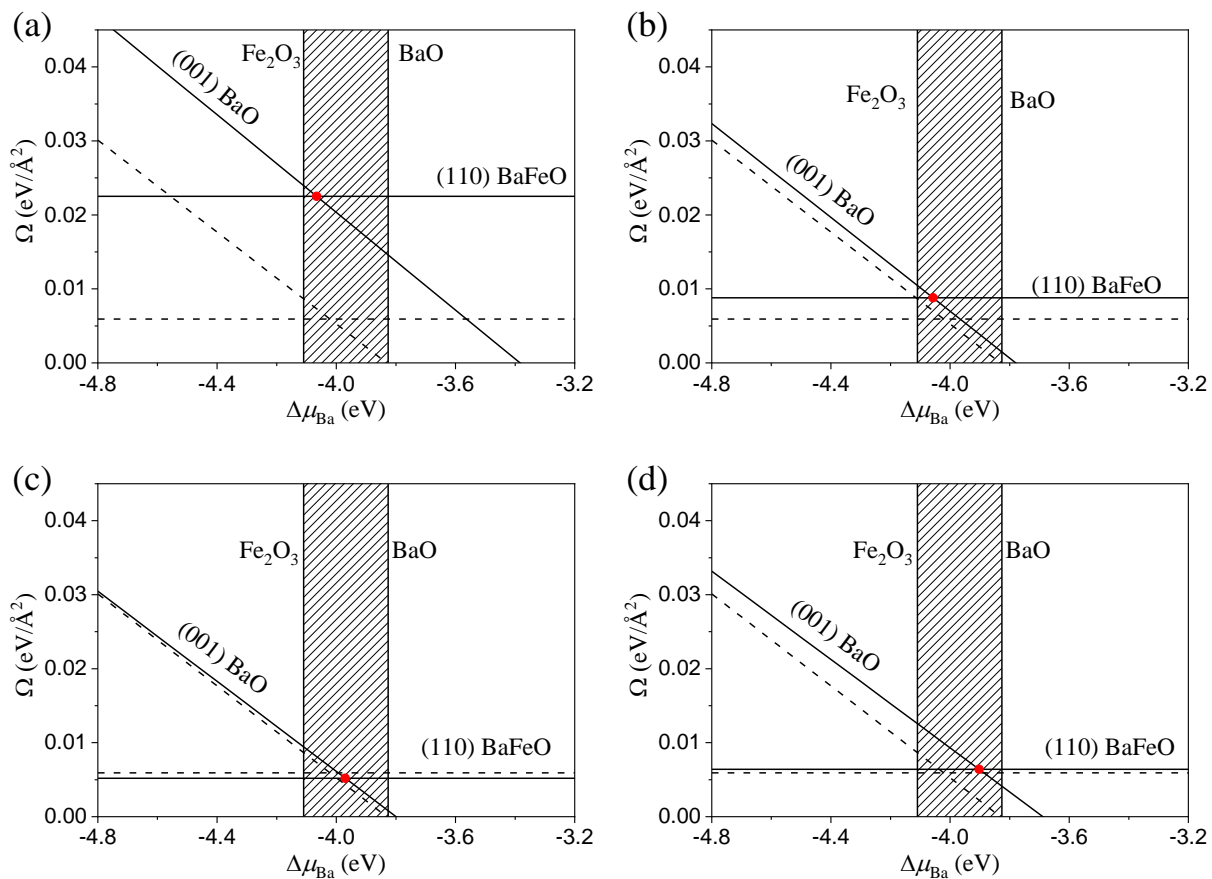


Figure S5 Surface Gibbs free energy Ω^i of (001) BaO and (110) BaFeO slabs at $p_{\text{O}_2} = 0.21$ atm and $T = 1100$ K under: (a) 3% compressive, (b) 1% compressive, (c) 1% tensile, and (d) 2% tensile applied ab -plane strains. The stable area is marked by a hatched pattern. The Ω^i 's computed at the applied strains are drawn as solid lines. The dashed lines correspond to the unstrained Ω^i 's. The intersection points between the (001) BaO and (110) BaFeO lines are shown in red.

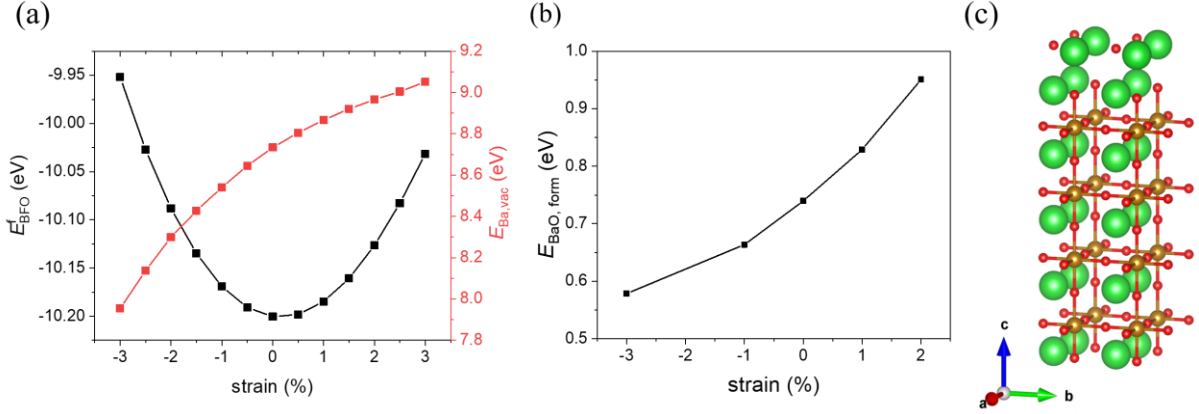


Figure S6 (a) Strain-dependent formation energies of BFO bulk per formula unit (left) and the vacancy formation energy of one Ba in $2 \times 2 \times 2$ supercell (right). (b) Calculated formation energy for forming one monolayer of BaO on the top surface of (001) BaO (c) as a function of applied biaxial strain.

The bulk formation energy, $E_{\text{BFO}}^{\text{f}}$, of BFO per formula unit is given by (S19). The Ba vacancy formation energy, $E_{\text{Ba,vac}}$, is calculated as

$$E_{\text{Ba,vac}} = (E_{\text{BFO}}^{\text{defect}} + E_{\text{Ba}}^{\text{bulk}}) - nE_{\text{BFO}}^{\text{bulk}} \quad (\text{S35})$$

where $E_{\text{BFO}}^{\text{defect}}$ is the energy of the $2 \times 2 \times 2$ supercell of BFO with one Ba vacancy, and $n = 8$ corresponds to the formula units in the $2 \times 2 \times 2$ supercell.

To evaluate the formation of one monolayer of BaO on the top surface, we chose (001) BaO as one example because AO-termination has been observed frequently in many perovskite oxides^{22, 23} as well as in our calculations (see Figures 2 and 3). Following the previous work²⁴, one monolayer of BaO was constructed on the top surface of (001) BaO (Figure S6c) to simulate the surface Ba enrichment. The formation energy, $E_{\text{BaO,form}}$, is calculated by

$$E_{\text{BaO,form}} = E_{\text{BaO+slab}}^{\text{perfect}} - E_{\text{slab}}^{\text{BaO}} - 4E_{\text{BaO}}^{\text{bulk}} \quad (\text{S36})$$

where $E_{\text{BaO+slab}}^{\text{perfect}}$ is the energy of the slab with one additional BaO layer, see Figure S6c, $E_{\text{slab}}^{\text{BaO}}$ is the energy of the perfect slab of (001) BaO as calculated before.

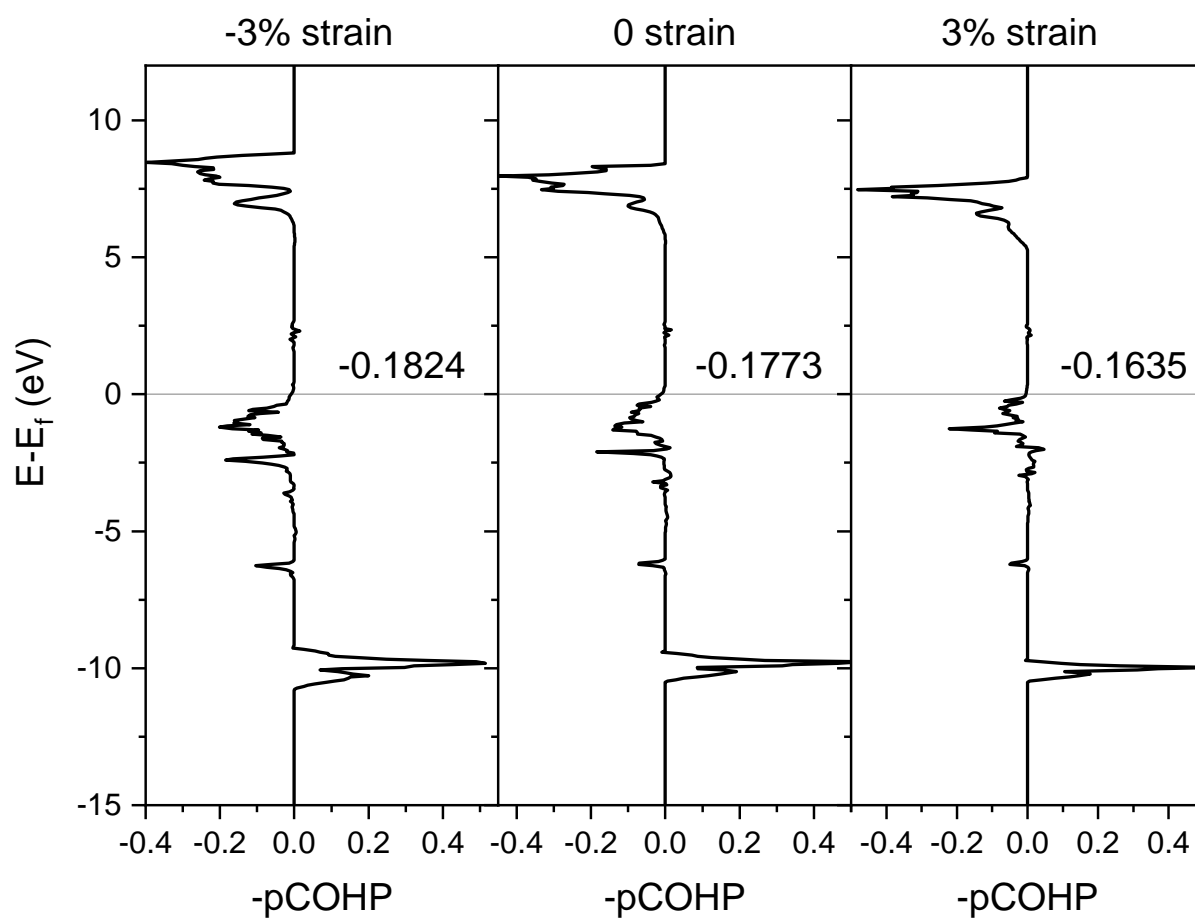


Figure S7 Calculated crystal orbital Hamilton populations (COHP) of Ba-O bond in the $2 \times 2 \times 2$ supercell of bulk BFO as a function of applied uniaxial strain. The integrated COHP value up to the Fermi level is also shown.

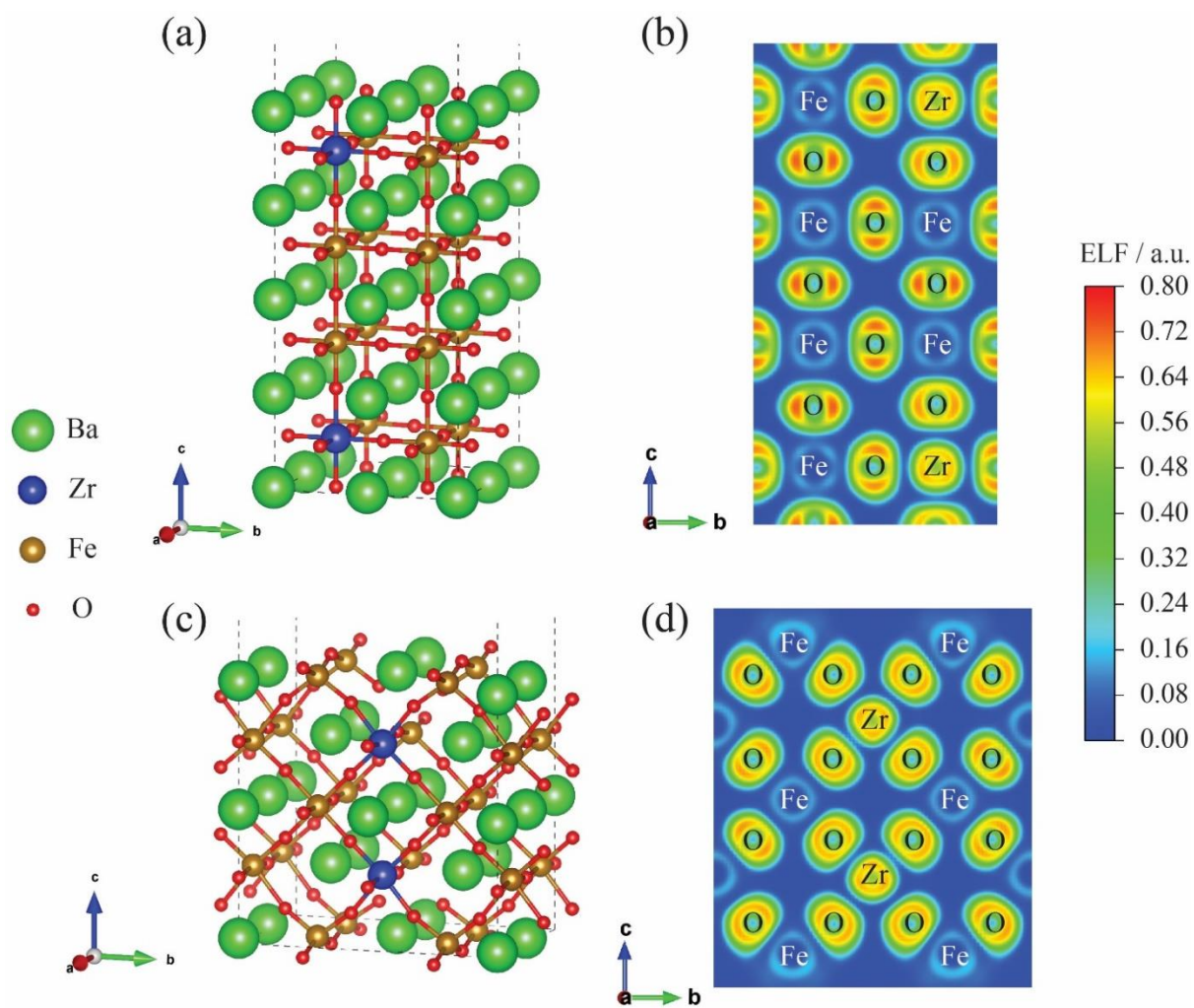


Figure S8 Relaxed BFZ slab models with (a) (001) BaO, (b) (110) BaFeO terminations. Plots of the ELF of the (c) (001) BaO- and (d) (110) BaFeO-terminated slabs.

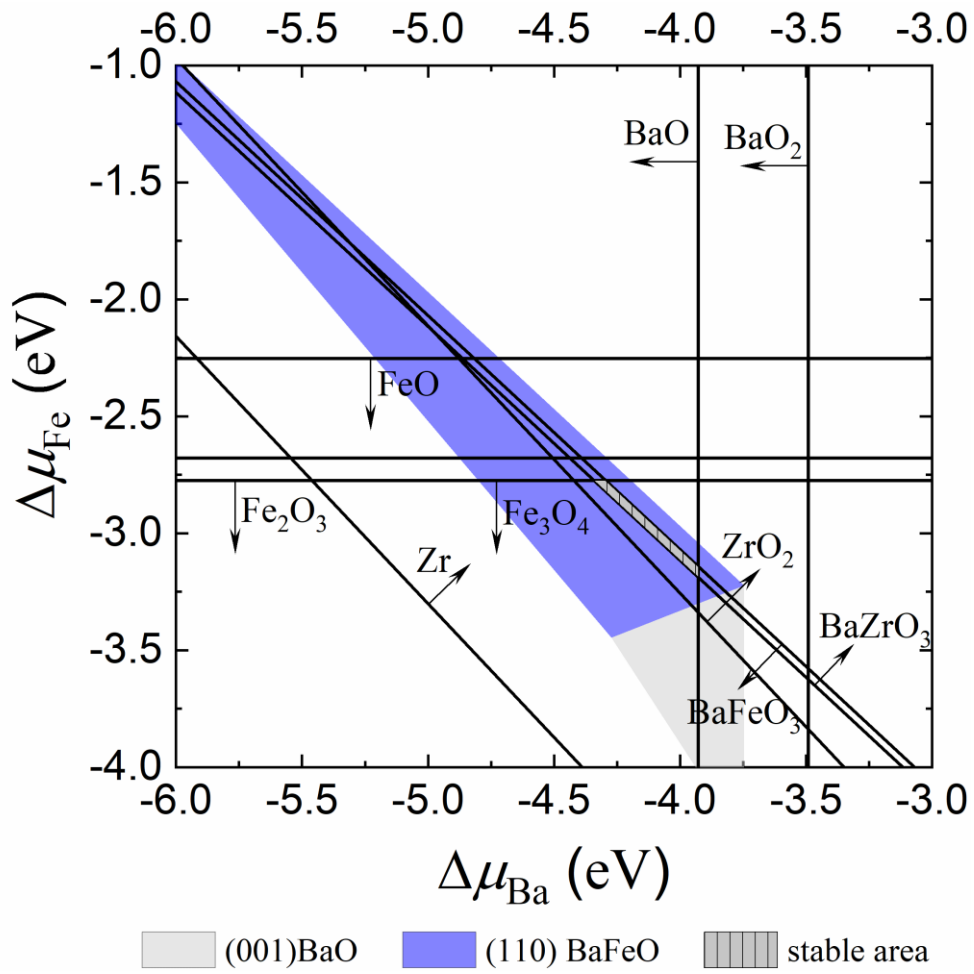


Figure S9 Surface phase diagram of BFZ as a function of $\Delta\mu_{\text{Ba}}$ and $\Delta\mu_{\text{Fe}}$ for $p_{\text{O}_2} = 0.21$ atm and $T = 1100$ K.

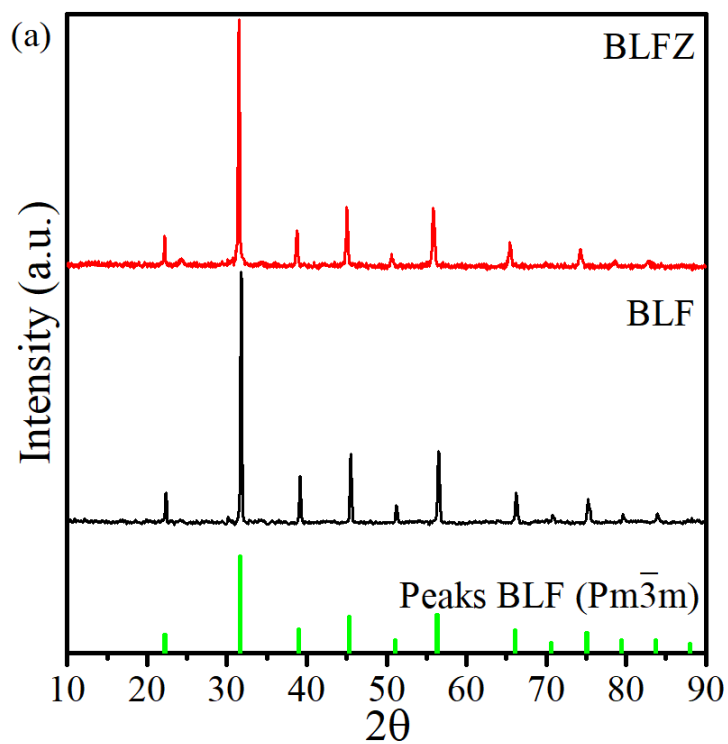


Figure S10 X-ray diffraction patterns of $Ba_{0.95}La_{0.05}FeO_{3-\delta}$ (BLF) and $Ba_{0.95}La_{0.05}Fe_{0.9}Zr_{0.1}O_{3-\delta}$ (BLFZ) powders.

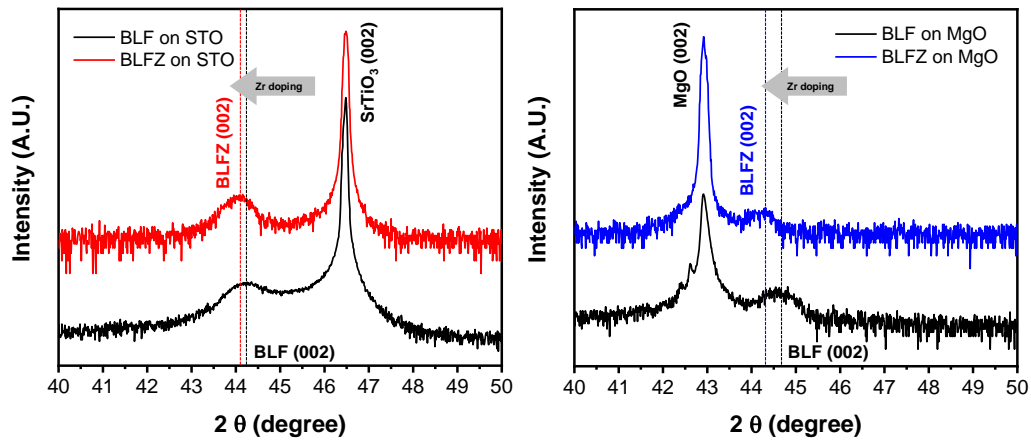


Figure S11 High-resolution thin-film X-ray diffraction results of epitaxial $\text{Ba}_{0.95}\text{La}_{0.05}\text{FeO}_{3-\delta}$ (BLF) and $\text{Ba}_{0.95}\text{La}_{0.05}\text{Fe}_{0.9}\text{Zr}_{0.1}\text{O}_{3-\delta}$ (BLFZ) thin films on single-crystal substrates (SrTiO_3 , STO (001) and MgO (002)). The graphs show the magnified regions (from 40° to 50°) in Figure 8a.

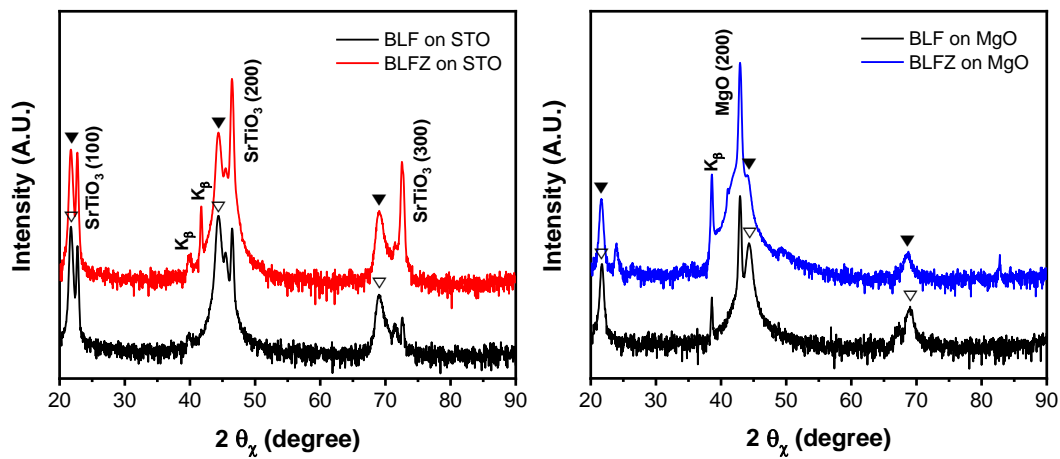


Figure S12 High-resolution thin-film X-ray diffraction results of epitaxial $\text{Ba}_{0.95}\text{La}_{0.05}\text{FeO}_{3-\delta}$ (BLF) and $\text{Ba}_{0.95}\text{La}_{0.05}\text{Fe}_{0.9}\text{Zr}_{0.1}\text{O}_{3-\delta}$ (BLFZ) thin films on single-crystal substrates (SrTiO_3 , STO (001) and MgO (002)). The graphs show in-plane diffraction patterns with (100) direction (2θ - ω scan). The BLFZ and BLF peaks are denoted with \blacktriangledown and \triangledown , respectively.

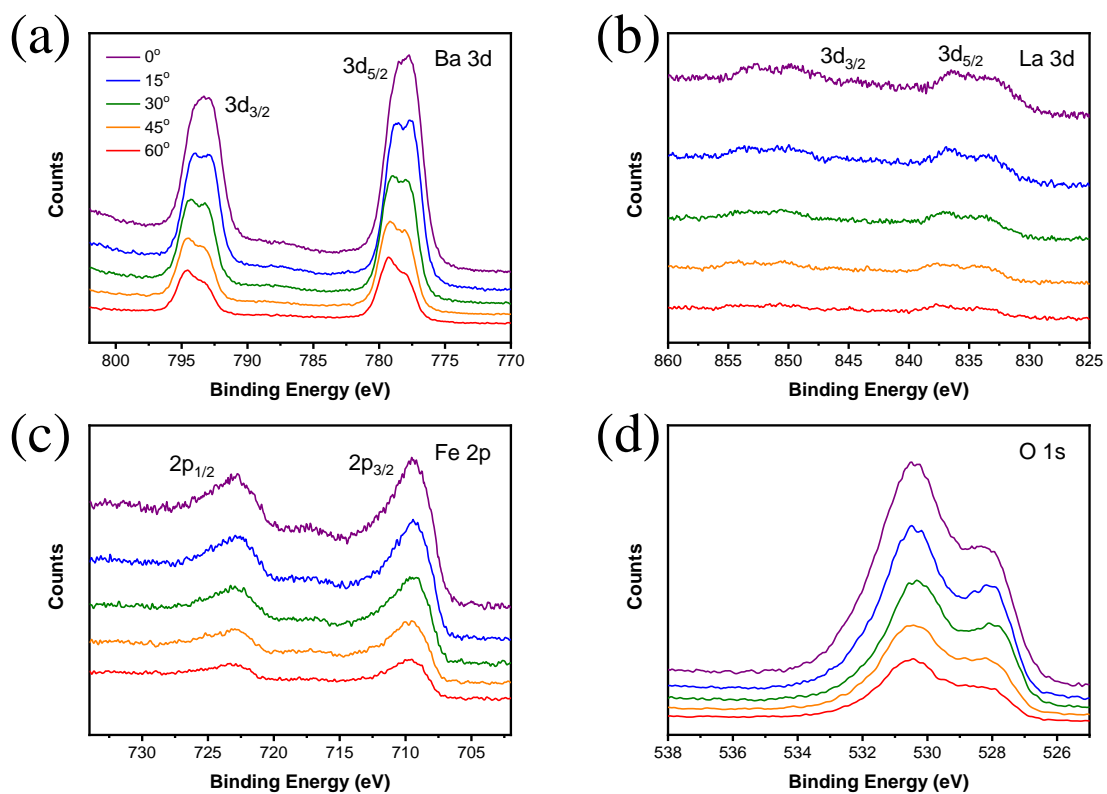


Figure S13 Angle-resolved X-ray photoelectron spectroscopy (AR-XPS) spectra of epitaxial BLF thin film on single-crystal SrTiO₃ varying emission angle. (a) Ba 3d, (b) La 3d, (c) Fe 2p, (d) O 1s.

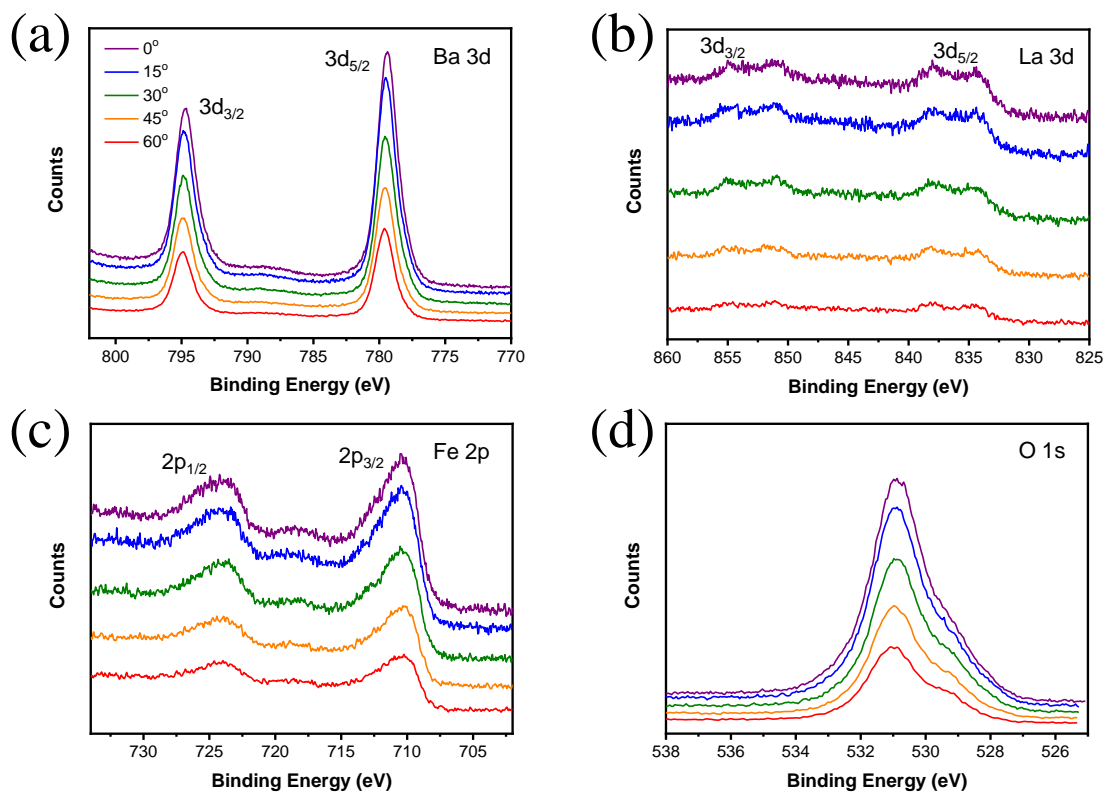


Figure S14 Angle-resolved X-ray photoelectron spectroscopy (AR-XPS) spectra of epitaxial BLF thin film on single-crystal MgO varying emission angle. (a) Ba 3d, (b) La 3d, (c) Fe 2p, (d) O 1s.

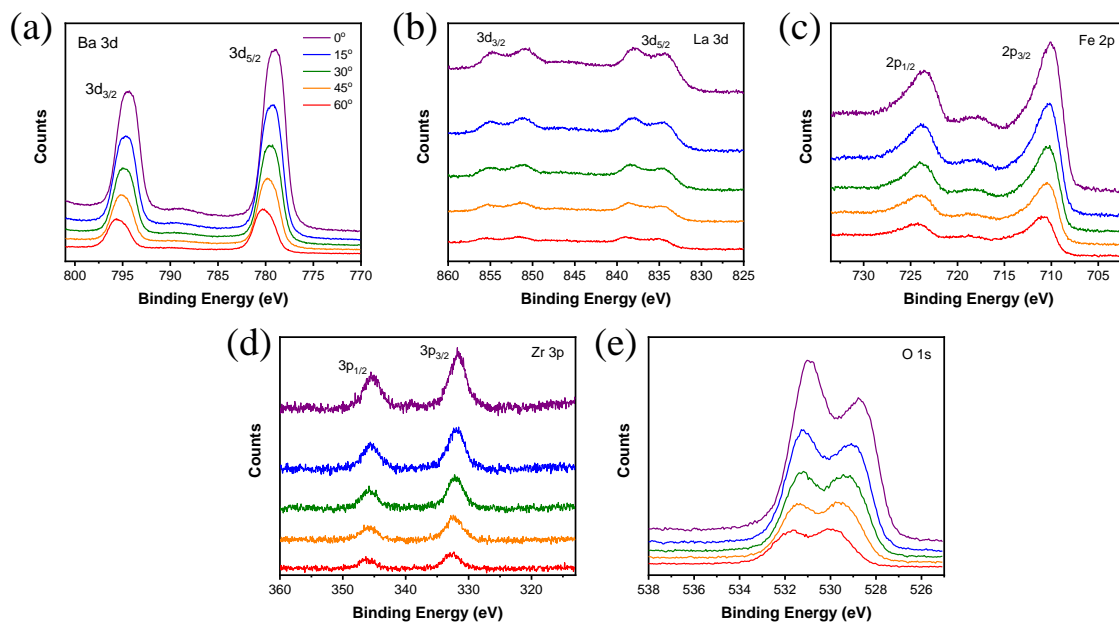


Figure S15 Angle-resolved X-ray photoelectron spectroscopy (AR-XPS) spectra of epitaxial BLFZ thin film on single-crystal SrTiO₃ varying emission angle. (a) Ba 3d, (b) La 3d, (c) Fe 2p, (d) Zr 3p, (e) O 1s.

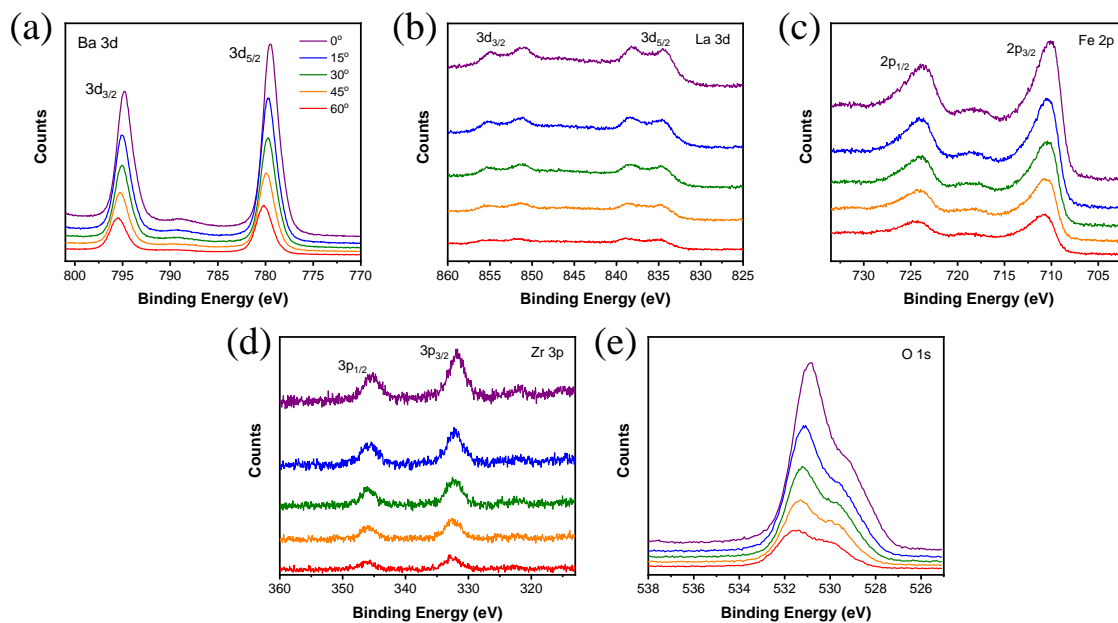


Figure S16 Angle-resolved X-ray photoelectron spectroscopy (AR-XPS) spectra of epitaxial BLFZ thin film on single-crystal MgO varying emission angle. (a) Ba 3d, (b) La 3d, (c) Fe 2p, (d) Zr 3p, (e) O 1s.

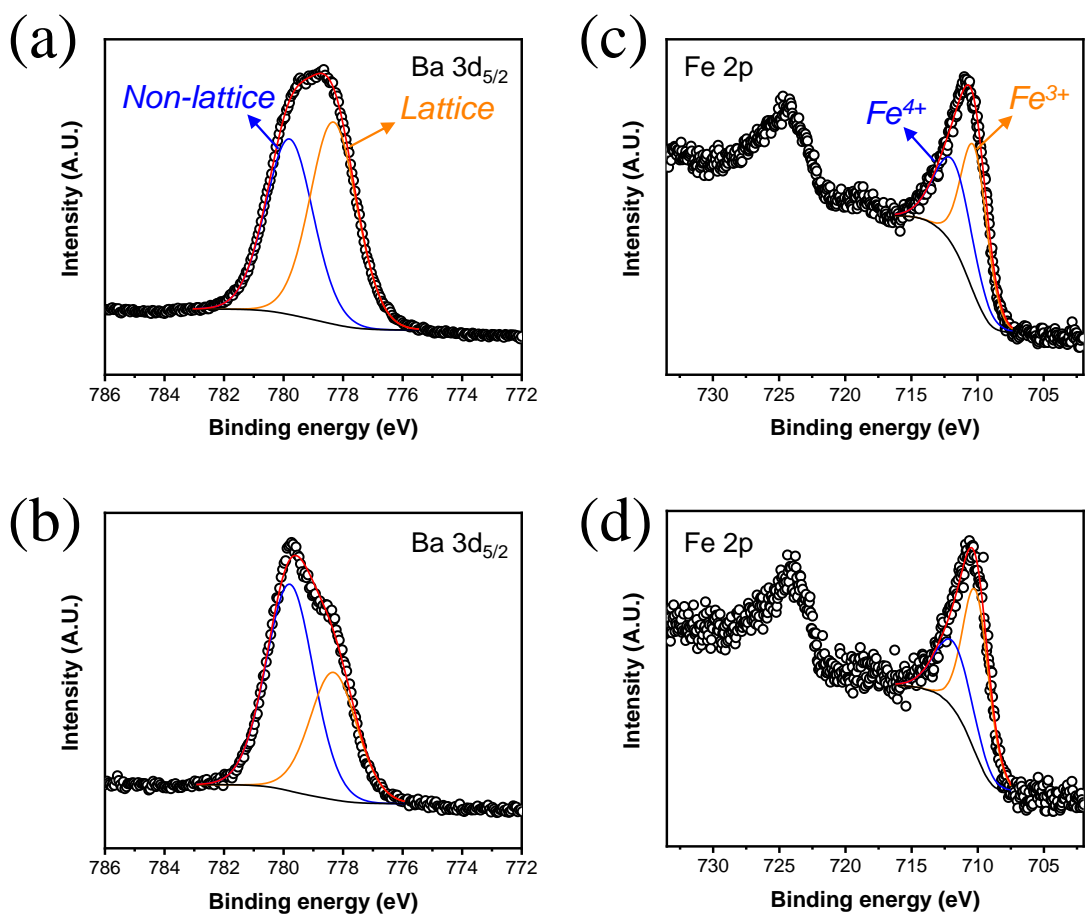


Figure S17 Fitted angle-resolved X-ray photoelectron spectroscopy (AR-XPS) spectra of epitaxial BLF thin film on single-crystal STO substrate varying emission angle. (a) Ba 3d_{5/2} at 0 degree, (b) Ba 3d_{5/2} at 60 degree, (c) Fe 2p at 0 degree, (d) Fe 2p at 60 degree.

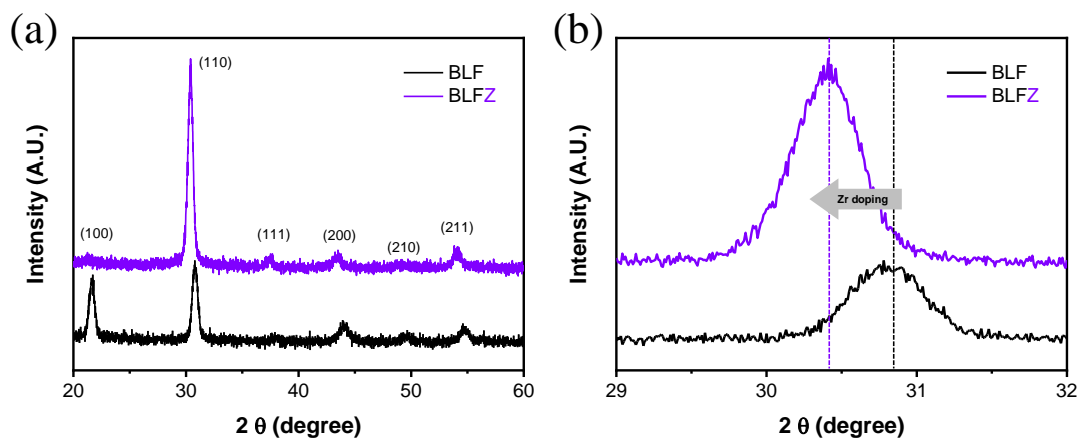


Figure S18 Thin-film X-ray diffraction patterns (2θ scan) of polycrystalline $\text{Ba}_{0.95}\text{La}_{0.05}\text{FeO}_{3-\delta}$ (BLF) and $\text{Ba}_{0.95}\text{La}_{0.05}\text{Fe}_{0.9}\text{Zr}_{0.1}\text{O}_{3-\delta}$ (BLFZ) thin films on Si substrate. (a) Full range, (b) Magnified range.

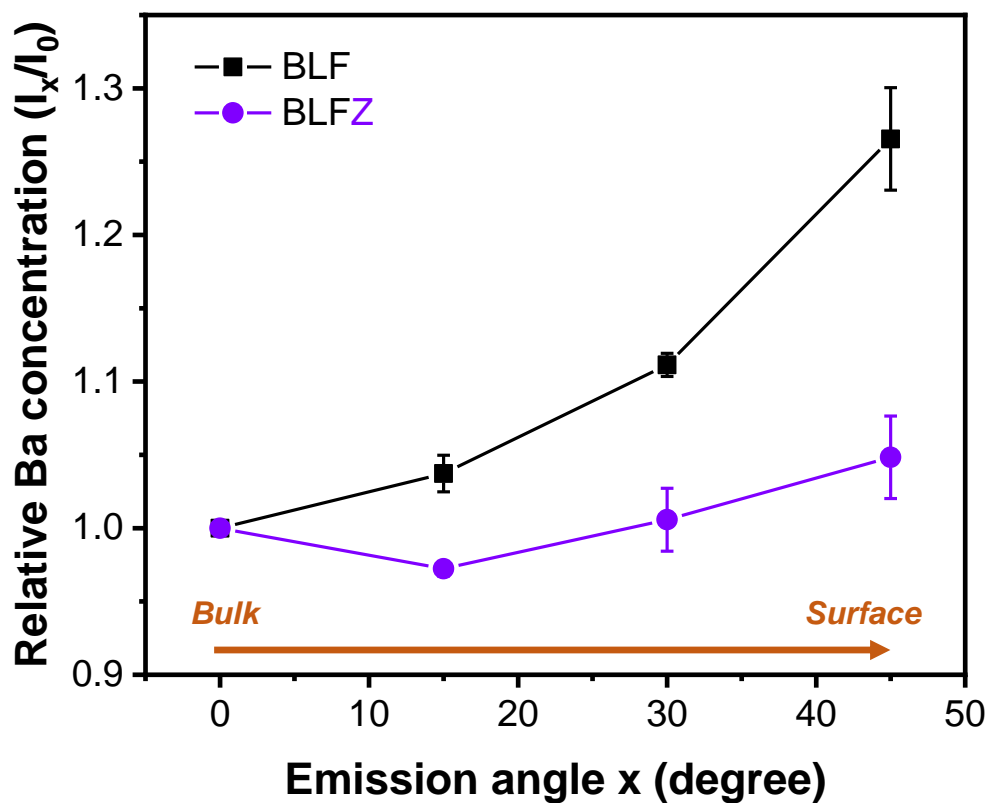


Figure S19 Surface chemistry of polycrystalline $\text{Ba}_{0.95}\text{La}_{0.05}\text{FeO}_{3-\delta}$ (BLF) and $\text{Ba}_{0.95}\text{La}_{0.05}\text{Fe}_{0.9}\text{Zr}_{0.1}\text{O}_{3-\delta}$ (BLFZ) thin films. The graph shows the relative Ba concentration of the films with various emission angles, x (from 0° to 45°) during angle-resolved X-ray photoelectron spectroscopy (AR-XPS) measurement. I_x denotes Ba/B-site ratio at x° .

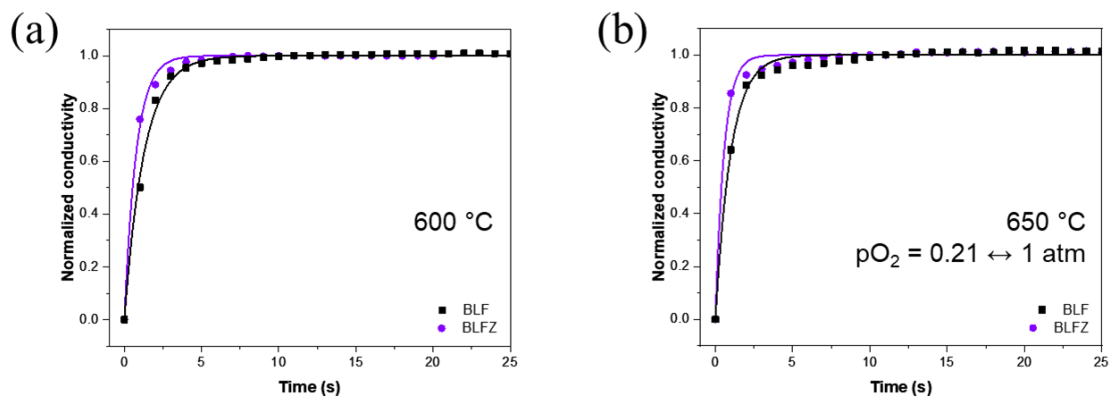


Figure S20 Surface oxygen exchange kinetics of polycrystalline $\text{Ba}_{0.95}\text{La}_{0.05}\text{FeO}_{3-\delta}$ (BLF) and $\text{Ba}_{0.95}\text{La}_{0.05}\text{Fe}_{0.9}\text{Zr}_{0.1}\text{O}_{3-\delta}$ (BLFZ) thin films on Al_2O_3 substrates. (a) Electrical conductivity relaxation curves of polycrystalline BLF and BLFZ thin films at 600 °C, and (b) at 650 °C with switching oxygen partial pressure from 0.21 atm to 1 atm. The thickness of the films is 500 nm.

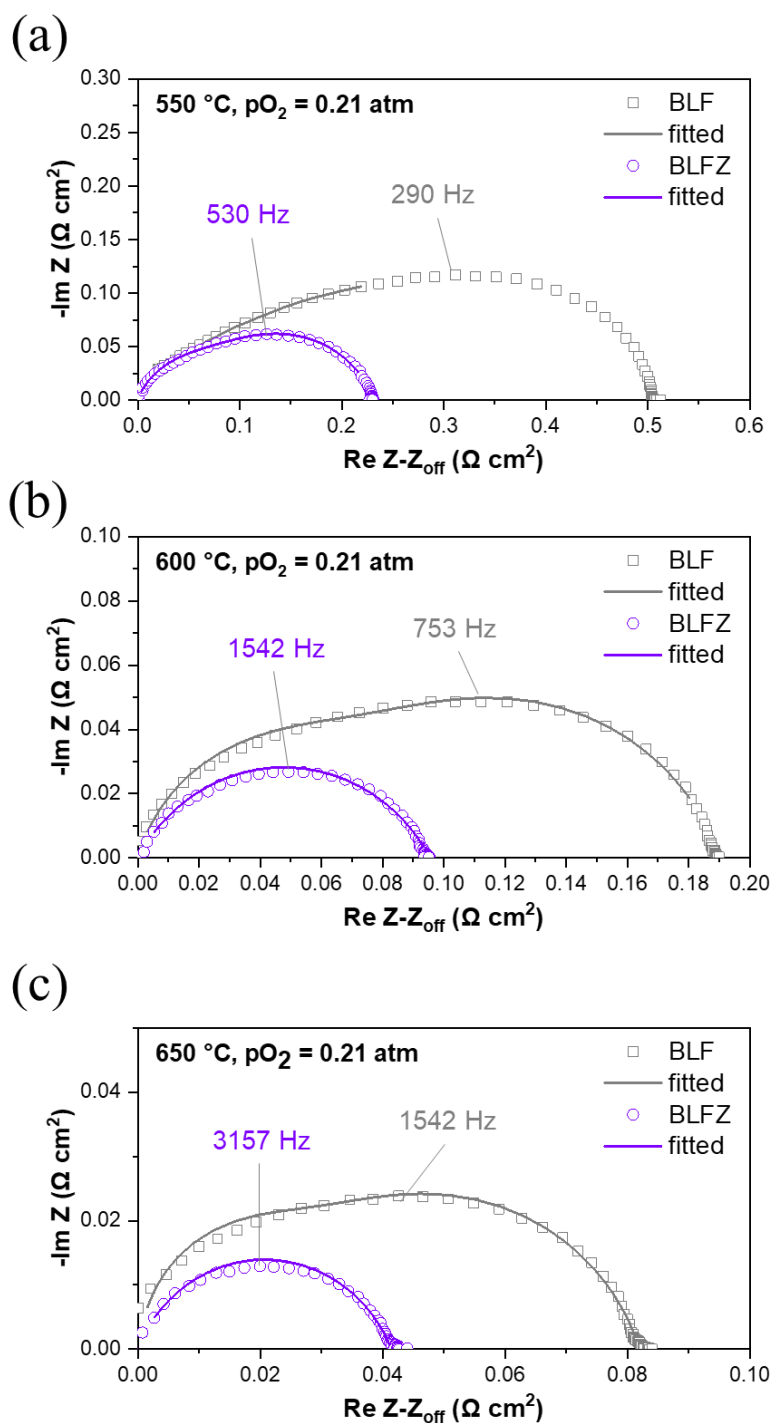


Figure S21 Surface oxygen exchange kinetics of polycrystalline $\text{Ba}_{0.95}\text{La}_{0.05}\text{FeO}_{3-\delta}$ (BLF) and $\text{Ba}_{0.95}\text{La}_{0.05}\text{Fe}_{0.9}\text{Zr}_{0.1}\text{O}_{3-\delta}$ (BLFZ) porous electrodes. Electrochemical impedance spectroscopy results of porous BLF and BLFZ symmetric cells (a) at 550 °C, (b) at 600 °C, and (c) at 650 °C under p_{O_2} value of 0.21 atm. 20 at% Sm doped $\text{CeO}_{2-\delta}$ was used as an electrolyte.

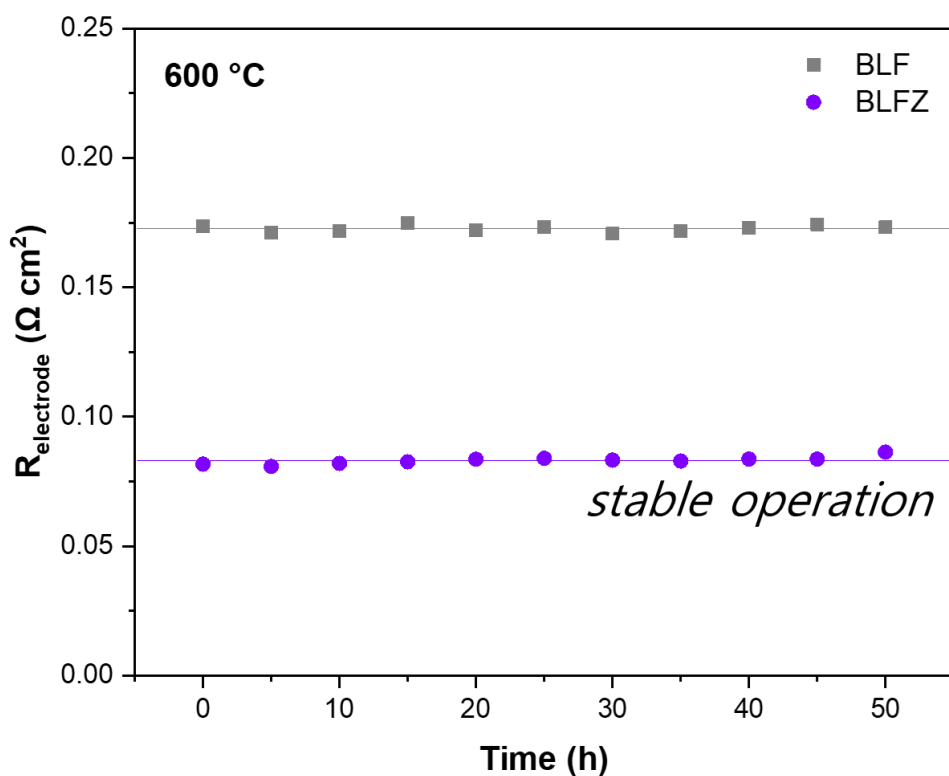


Figure S22 Durability test results of polycrystalline $\text{Ba}_{0.95}\text{La}_{0.05}\text{FeO}_{3-\delta}$ (BLF) and $\text{Ba}_{0.95}\text{La}_{0.05}\text{Fe}_{0.9}\text{Zr}_{0.1}\text{O}_{3-\delta}$ (BLFZ) porous electrodes at 600 °C under p_{O_2} value of 0.21 am. 20 at% Sm doped $\text{CeO}_{2-\delta}$ was used as an electrolyte. Both BLF and BLFZ show stable operations.

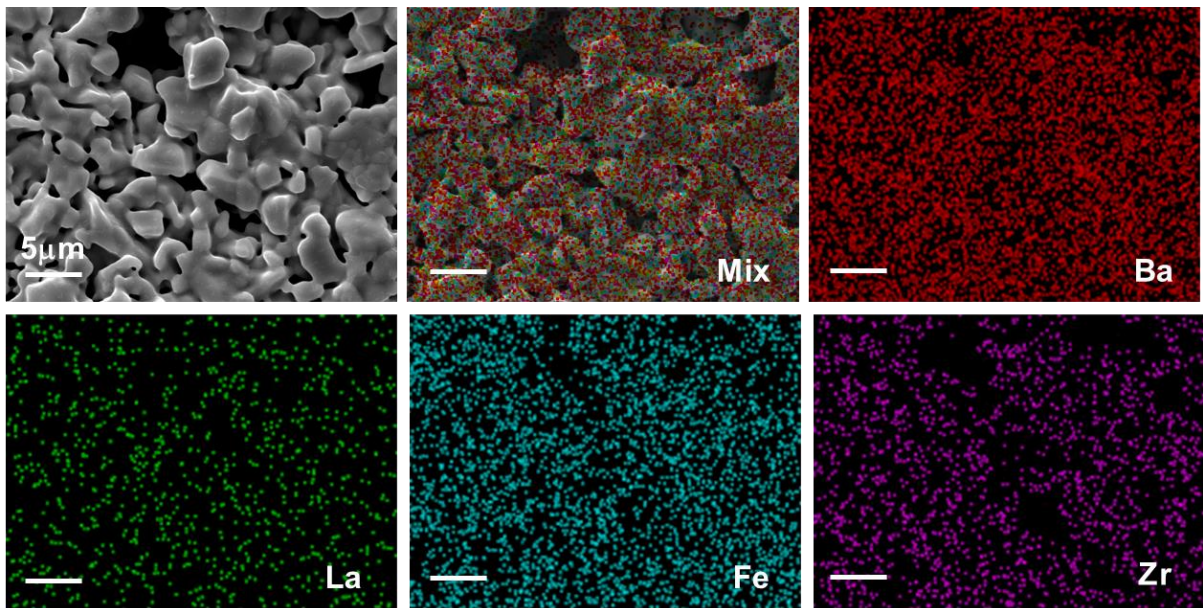


Figure S23 Surface morphology SEM photo of BLFZ cathode.

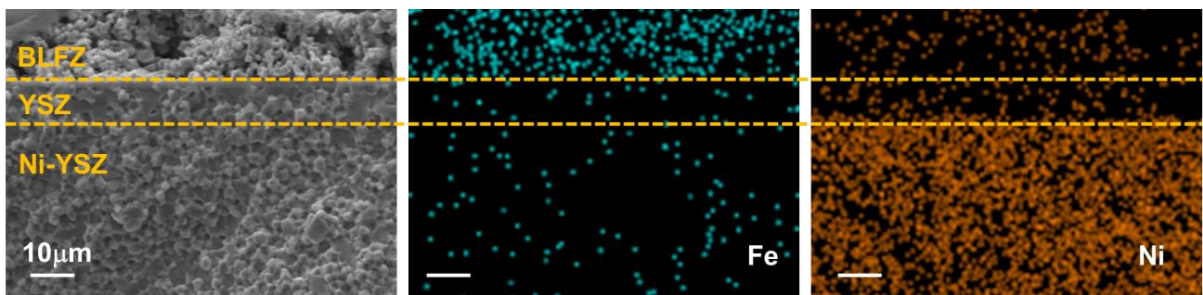


Figure S24 Cross-sectional SEM photo of SOFC with the configuration of Ni-YSZ|YSZ|BLFZ.

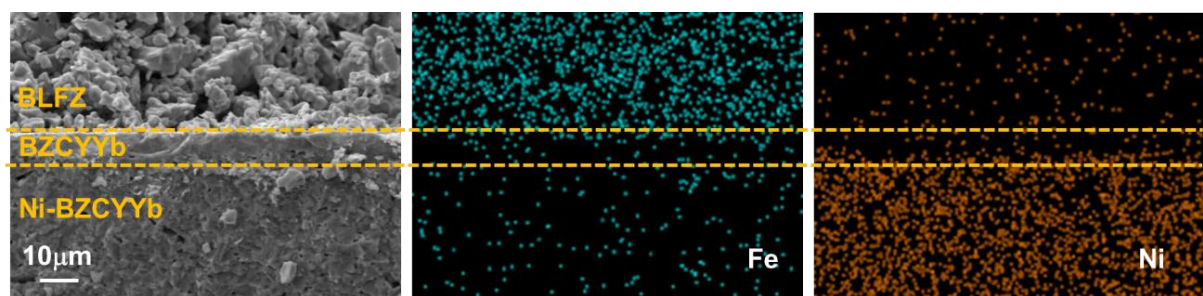


Figure S25 Cross-sectional SEM photo of PCFC with the configuration of Ni-BZCYYb|BZCYYb|BLFZ.

Table S1 Calculated formation energies of oxides per formula unit. Experimental values are also presented.²⁵

Material	Calculated E^f (eV)	Experimental E^f (eV)
BaO	-4.97	-5.68
BaO ₂	-5.58	-6.57
Fe ₂ O ₃	-8.74	-8.56
FeO	-2.83	-2.82

Table S2 Calculated Schottky formation energy E_{Schottky} for (001) BaO and (110) BaFeO in different locations

E_{Schottky}	(001) BaO	(110) BaFeO
Bulk (mirror plane)	4.64	4.12
layer III	7.64	6.85
Top surface (layer I)	4.36	5.78

Table S3 Calculated Bader charge and the Ba-O bond length for the slab models studied.

Layer	Atomic charge (e)			
	Ba	Zr	Fe	O
BFO, (001) BaO:				
I	1.50			-1.19
II			1.74	-1.14
III	1.59			-1.08
BFO, (001) BaO tensile 2%:				
I	1.51			-1.13
II			1.74	-1.16
III	1.56			-1.10
BFZ, (110) BaO:				
I	1.52			-1.21
II		2.45	1.61	-1.13
III	1.58			-1.15
BFO, (110) BaFeO:				
I	1.51		1.54	-1.30
II				-1.24
III	1.54		1.73	-1.25
BFO, (110) BaFeO tensile 2%:				
I	1.49		1.54	-1.30
II				-1.24
III	1.55		1.74	-1.23
BFZ, (110) BaFeO:				
I	1.51			-1.29
II				-1.26
III	1.56	2.46	1.73	-1.25

Table S4 Lattice parameter of BLF and BLFZ from the XRD measurement at room temperature.

Material	Lattice Parameter (Å)
BLF	4.02
BLFZ	4.05

Table S5 Bulk composition of $\text{Ba}_{0.95}\text{La}_{0.05}\text{FeO}_{3-\delta}$ (BLF) and $\text{Ba}_{0.95}\text{La}_{0.05}\text{Fe}_{0.9}\text{Zr}_{0.1}\text{O}_{3-\delta}$ (BLFZ) powder measured by X-Ray fluorescence (XRF) and thin films using inductively coupled plasma-mass-spectrometry, respectively.

Material	Cation element	Nominal	Powder	Thin film
BLF	Ba	47.50	47.76	51.57
	La	2.50	2.07	2.22
	Fe	50.00	50.17	46.21
BLFZ	Ba	47.50	47.70	51.48
	La	2.50	2.34	2.97
	Fe	45.00	45.10	41.15
	Zr	5.00	4.86	4.40

Table S6 Comparison of materials and performance with SOFCs reported in the literature.

Cathode	Electrolyte	Electrolyte thickness (μm)	Temperature ($^{\circ}\text{C}$)	PPD (mW cm^{-2})	Ref.
Ba_{0.95}La_{0.05}Fe_{0.9}Zr_{0.1}O_{3-δ} (BLFZ)	Yttria-stabilized zirconia (YSZ)	12	850	1802	This work
			800	1315	
			750	810	
BaCo _{0.4} Fe _{0.4} Zr _{0.1} Y _{0.1} O _{2.95-δ} F _{0.05} (BCFZYF)	Yttria-stabilized zirconia (YSZ)	15.4	800	786	26
			750	541	
			700	334	
PrBaCo ₂ O _{5+δ} – Gd _{0.1} Ce _{0.9} O _{2-δ} (PBC–GDC)	La _{0.8} Sr _{0.2} Ga _{0.8} Mg _{0.2} O _{3-δ} (LSGM)	300	850	1302	27
			800	1117	
			750	938	
			700	746	
(Ba _{0.95} La _{0.05}) _(1-10%) FeO _{3-δ} (BLF-D10)	Yttria-stabilized zirconia (YSZ)	25	800	614	28
			750	502	
			700	401	
La _{0.6} Sr _{0.4} Co _{0.2} Fe _{0.8} O _{3-δ} (LSCF)	La _{0.8} Sr _{0.2} Ga _{0.8} Mg _{0.2} O _{3-δ} (LSGM)	180	850	1090	29
			800	810	
			750	500	
			700	300	
Ba _{0.9} Co _{0.4} Fe _{0.4} Zr _{0.1} Y _{0.1} O _{3-δ}	Yttria-stabilized zirconia (YSZ)	10	800	730	30
			750	522	
			700	336	

Table S7 Comparison of materials and performance with PCFCs reported in the literature.

Cathode	Electrolyte	Electrolyte thickness (μm)	Temperature ($^{\circ}\text{C}$)	PPD (mW cm^{-2})	Ref.
Ba_{0.95}La_{0.05}Fe_{0.9}Zr_{0.1}O_{3-δ} (BLFZ)	BaZr_{0.1}Ce_{0.7}Y_{0.1}Yb_{0.1}O_{3-δ} (BZCYYb)	10	700	1316	This work
			650	992	
			600	708	
BaCe _{0.6} Zr _{0.3} Y _{0.1} O _{3-δ} (BCZY631)- BaCo _{0.4} Fe _{0.4} Zr _{0.1} Y _{0.1} O _{3-δ} (BCFZY0.1)	BaZr _{0.1} Ce _{0.7} Y _{0.1} Yb _{0.1} O _{3-δ} (BZCYYb)	15-50	600	648	31
BaCo _{0.4} Fe _{0.4} Zr _{0.2} O _{3-δ}	BaZr _{0.1} Ce _{0.7} Y _{0.1} Yb _{0.1} O _{3-δ} (BZCYYb)	30	650	232	32
			600	225	
			550	200	
BCZY	BaZr _{0.1} Ce _{0.7} Y _{0.1} Yb _{0.1} O _{3-δ} (BZCYYb)	7	550	440	33
Sr _{0.9} Ce _{0.1} Fe _{0.8} Ni _{0.2} O _{3-δ} (SCFN)	BaZr _{0.1} Ce _{0.7} Y _{0.1} Yb _{0.1} O _{3-δ} (BZCYYb)	26	650	745	34
			600	531	
			550	347	
Sr _{0.9} Ce _{0.1} Fe _{0.8} Ni _{0.2} O _{3-δ} (SCFN)	BaZr _{0.1} Ce _{0.7} Y _{0.1} Yb _{0.1} O _{3-δ} (BZCYYb)	30	700	586	35
			650	435	
			600	320	

Reference

1. L. Yang, S. Wang, K. Blinn, M. Liu, Z. Liu, Z. Cheng and M. Liu, *Science*, 2009, **326**, 126-129.
2. G. Kresse and J. Furthmüller, *Physical Review B*, 1996, **54**, 11169.
3. G. Kresse and J. Furthmüller, *Computational Materials Science*, 1996, **6**, 15-50.
4. P. E. Blöchl, *Physical Review B*, 1994, **50**, 17953.
5. J. P. Perdew, K. Burke and M. Ernzerhof, *Physical Review Letters*, 1996, **77**, 3865.
6. S. L. Dudarev, G. A. Botton, S. Y. Savrasov, C. J. Humphreys and A. P. Sutton, *Physical Review B*, 1998, **57**, 1505-1509.
7. Y.-L. Lee, J. Kleis, J. Rossmeisl, Y. Shao-Horn and D. Morgan, *Energy & Environmental Science*, 2011, **4**, 3966-3970.
8. Z. M. Baiyee, C. Chen and F. Ciucci, *Physical Chemistry Chemical Physics*, 2015, **17**, 23511-23520.
9. C. Chen and F. Ciucci, *Chemistry of Materials*, 2016, **28**, 7058-7065.
10. N. Hayashi, T. Yamamoto, H. Kageyama, M. Nishi, Y. Watanabe, T. Kawakami, Y. Matsushita, A. Fujimori and M. Takano, *Angewandte Chemie International Edition*, 2011, **50**, 12547-12550.
11. K. Reuter and M. Scheffler, *Physical Review B*, 2001, **65**, 035406.
12. J. Padilla and D. Vanderbilt, *Physical Review B*, 1997, **56**, 1625.
13. K. Johnston, M. R. Castell, A. T. Paxton and M. W. Finnis, *Physical Review B*, 2004, **70**, 085415.
14. F. Bottin, F. Finocchi and C. Noguera, *Physical Review B*, 2003, **68**, 035418.
15. K. Reuter and M. Scheffler, *Applied Physics A*, 2004, **78**, 793-798.
16. X.-G. Wang, A. Chaka and M. Scheffler, *Physical Review Letters*, 2000, **84**, 3650.
17. X.-G. Wang, W. Weiss, S. K. Shaikhutdinov, M. Ritter, M. Petersen, F. Wagner, R. Schlögl and M. Scheffler, *Physical Review Letters*, 1998, **81**, 1038.
18. E. Heifets, J. Ho and B. Merinov, *Physical Review B*, 2007, **75**.
19. S. Zhang, N. Han and X. Tan, *RSC Advances*, 2015, **5**, 760-769.
20. E. Heifets, S. Piskunov, E. A. Kotomin, Y. F. Zhukovskii and D. E. Ellis, *Physical Review B*, 2007, **75**, 115417.
21. M. W. Chase, *NIST-JANAF Thermochemical Tables*, American Institute of Physics, Washington DC, 4th edn., 1998.

22. A. Staykov, H. Téllez, T. Akbay, J. Druce, T. Ishihara and J. Kilner, *Chemistry of Materials*, 2015, **27**, 8273-8281.
23. J. Druce, H. Téllez, M. Burriel, M. D. Sharp, L. J. Fawcett, S. N. Cook, D. S. McPhail, T. Ishihara, H. H. Brongersma and J. A. Kilner, *Energy & Environmental Science*, 2014, **7**, 3593-3599.
24. B. Koo, H. Kwon, Y. Kim, H. G. Seo, J. W. Han and W. Jung, *Energy & Environmental Science*, 2018, **11**, 71-77.
25. O. Kubaschewski, C. B. Alcock and P. Spencer, *Materials thermochemistry*, Pergamon Press, 1993.
26. W. Wang, X. Zhang, D. Zhang, Q. Zeng, Y. Jiang and B. Lin, *Ceramics International*, 2020, **46**, 23964-23971.
27. Y. Zhang, L. Shen, Y. Wang, Z. Du, B. Zhang, F. Ciucci and H. Zhao, *Journal of Materials Chemistry A*, 2022, **10**, 3495-3505.
28. A. Belotti, Y. Wang, A. Curcio, J. Liu, E. Quattrocchi, S. Pepe and F. Ciucci, *International Journal of Hydrogen Energy*, 2022, **47**, 1229-1240.
29. Y. Yang, Y. Wang, Z. Yang, Z. Lei, C. Jin, Y. Liu, Y. Wang and S. Peng, *Journal of Power Sources*, 2019, **438**, 226989.
30. W. Wang, X. Zhang, K. Khan, H. Wu, D. Zhang, Y. Yang, Y. Jiang and B. Lin, *International Journal of Hydrogen Energy*, 2021, **46**, 5593-5603.
31. C. Duan, J. Tong, M. Shang, S. Nikodemski, M. Sanders, S. Ricote, A. Almansoori and R. O'Hayre, *Science*, 2015, **349**, 1321-1326.
32. M. Shang, J. Tong and R. O'Hayre, *RSC Advances*, 2013, **3**, 15769-15775.
33. R. J. Braun, A. Dubois, K. Ferguson, C. Duan, C. Karakaya, R. J. Kee, H. Zhu, N. P. Sullivan, E. Tang, M. Pastula, A. Wood, T. Joia and R. O'Hayre, *ECS Transactions*, 2019, **91**, 997-1008.
34. Y. Song, J. Liu, Y. Wang, D. Guan, A. Seong, M. Liang, M. J. Robson, X. Xiong, Z. Zhang, G. Kim, Z. Shao and F. Ciucci, *Advanced Energy Materials*, 2021, **11**, 2101899.
35. Y. Wang, Y. Song, J. Liu, K. Yang, X. Lin, Z. Yang and F. Ciucci, *Advanced Energy and Sustainability Research*, 2022, **3**, 2100171.